Characterization of superconducting parametric amplifiers

Master's thesis

Duiquan Zheng

June 3, 2022

This report is in partial fulfillment of the Master program at Delft University of Technology.

Student:	Duiquan Zheng (5213509)
Daily Supervisor:	Lukas Johannes Splitthoff
Responsible Thesis Supervisor:	Christian Kraglund Andersen
Institute:	QuTech/TU Delft

Contents

Abstract

Superconducting parametric amplifiers have been developed for fast and high fidelity single shot readout of superconducting qubits. The nonliniarity required for those amplifiers is either based on various types of Josephson junctions or high kinetic inductance materials. The Andersen Lab currently develops a novel type of superconducting parametric amplifiers based on superconducting-semiconducting hybrid nanowires, which will allow for in-situ tuning of the amplifier characteristics with a gate voltage.

To prepare for the required performance tests of nanowire-based parametric amplifiers, we characterize a commercially available travelling wave parametric amplifier in terms of 5 figures of merit: gain, bandwidth, saturation power, noise temperature and quantum efficiency. We find a state of the art amplifier performances, but also detect several hardware problems in the measurement setup, which must be solved prior to further test. The method implemented here can be generalized to the characterization of all types superconducting parametric amplifiers.

Chapter 1

Introduction

One of the most promising routes towards building a quantum computer is using the architecture of superconducting circuits [1]. Among other imperfections in current devices, the readout of superconducting qubits needs to be improved to reach higher fidelities. Recent developments of superconducting parametric amplifiers overcame the measurement problem of measuring weak microwave signals [2]. These amplifiers typically feature sufficient gain, bandwidth, saturation power and little added noise.

The amplification process relies on the wave mixing of the signal tone with the pump tone mediated by a nonlinear circuit elements, during which the energy from the pump is converted into signal photons, thereby providing gain. Most commonly, Josephson junctions or high kinetic inductance materials are used as nonlinear circuit element, thus the amplifiers are called Josephson parametric amplifier (JPA) [2] or kinetic inductance parametric Amplifier (KIPA) [3, 4].

Although Josephson parametric amplifiers achieve near-quantum limited noise performance[4], they have many limitations, including narrow bandwidth and low saturation power. While the narrow bandwidth originates from the narrow linewidth of the resonator forming the JPA, the low saturation power is mainly linked to the critical current of the Josephson junction [5, 2]. These limitations could be problematic in up-scaling of superconducting circuits, where multiple qubits need to be read out simultaneously [6, 7]. Despite the inherent problem of JPAs, they are still widely used.

The Andersen Lab is currently developing a novel type of kinetic inductance parametric amplifier, which is based on hybrid superconductor-semiconductor nanowires. The key motivation for the use of nanowires is

their gate voltage tunability. As apposed to current or flux-driven JPA, multiple voltage-tuned parametric amplifier can be positioned more closely in the same circuit due to reduced inter device cross-talk. Moreover, this property facilitates the tuning of the parametric amplifier since it alleviates the need for large currents or fluxes in the vicinity of the JPA [8, 9]. Moreover, these nanowire parametric amplifier (NPA) are magnetic field compatible [10]. This compatibility can be important for hybrid systems where circuit QED is used to read out spin qubits[11].

Because superconducting parametric amplifier works in milli-Kelvin temperature environment and works with very weak microwave signal(only a few photons), it is not easy to directly detect the input and output power of the amplifier[12]. However, this problem could be circumvented by installing the parametric amplifier into a complete qubit readout chain[13, 14, 15, 16, 5, 17], where the gain, bandwidth, saturation power, noise temperature and quantum efficiency could all be characterized.

In preparation for the performance tests of this novel nanowire parametric amplifier that is being developed by Lukas Splitthoff in Andersen Lab at QuTech, we characterize a commercially available travelling wave parametric amplifier (TWPA), which had already been installed and used in one of the available measurement stations. In this thesis, we established a general measurement protocol to test the amplifier performance. We reported the gain, bandwidth and saturation power of the TWPA. Using a transmon qubit, we quantified the quantum efficiency of the entire readout chain. We found hardware problems, which must be solved prior to further tests.

Chapter 2

Theory

We need quantum limited amplifier to improve the measurement in circuit QED. Here we characterize the performance of amplifier by measuring the quantum measurement efficiency of the system. In this chapter, we presented and explained the basic figures of a general amplifier, the readout of Transmon qubit, and the concept of quantum efficiency.

2.1 Superconducting parametric amplifier

Superconducting parametric amplifiers are also referred as a quantum-limited amplifier, the type of amplifiers whose intrinsic noise reaches the lower limit given by quantum mechanics. For superconducting parametric amplifier, the environmental source of noise is reduced to its minimum by working in a cryogenic environment($k_bT \ll \hbar\omega$) where the thermal fluctuations are canceled.

2.1.1 Introduction to TWPA

One example of quantum-limited amplifier is Josephson traveling wave parametric amplifier (JTWPA). It is widely used to amplify microwave signals[2]. JTWPA is made up of transmission lines with series-connected Josephson junctions, as shown in Fig.2.1. By injecting a strong pump tone(at frequency f_p), the signal tone(at frequency f_s) will be amplified while traveling through JTWPA.

Fig.2.1(b) describes a general amplifying circuit of JTWPA[2]. In this

configuration, a microwave signal comes out of a qubit chip, goes into a cryogenic isolator, then a directional coupler, where an additional pump tone is introduced. While pump tone and signal tone are traveling through TWPA together, a portion of the energy of the pump tone is converted into that of the signal tone, with an additional idler tone generated. When JTWPA is set into "four-wave mixing" configuration, the pump tone, signal tone, and idler tone together follow a frequency relation $2f_p = f_s + f_i$.

Fig.2.1(c) describes a typical amplification behavior of JTWPA[15]. JTWPA could maintain a good power gain over a wide range of signal frequency[15, 12, 6]. Variations in the gain on the order of 2-3dB would most like come from imperfect impedance matching inside JTWPA. Notice that there exists a dip in the middle of the gain profile, and a localized peak within that dip. The localized peak corresponds to the pump frequency, the two dips nearby correspond to the reflection of either signal or idler tone when measuring close to the pump frequency[6].

2.1.2 Gain, bandwidth, and saturation power

Here we explain the three basic figures of merit for a general amplifier: gain, bandwidth and saturation power.

Gain

As explained in Subsec.2.1.1, signal tone is amplified only when it travels through TWPA with an additional power source pump tone. In other words, by turning pump tone on/off, we could measure the signal amplified/un-amplified by TWPA. Therefore, the power gain provided by TWPA can defined as

$$G = \frac{P_{Amplified}}{P_{Not\ amplified}}, \tag{2.1}$$

where $P_{Amplified}$ and $P_{Not\ amplified}$ denotes the power of the amplified/un-amplified signal. Because superconducting circuits operate at GHz frequencies, standard microwave techniques could be used to measure the signal amplitudes, i.e., in the units of Voltage. Using unit of decibels, Eq.2.1 is rewritten as:

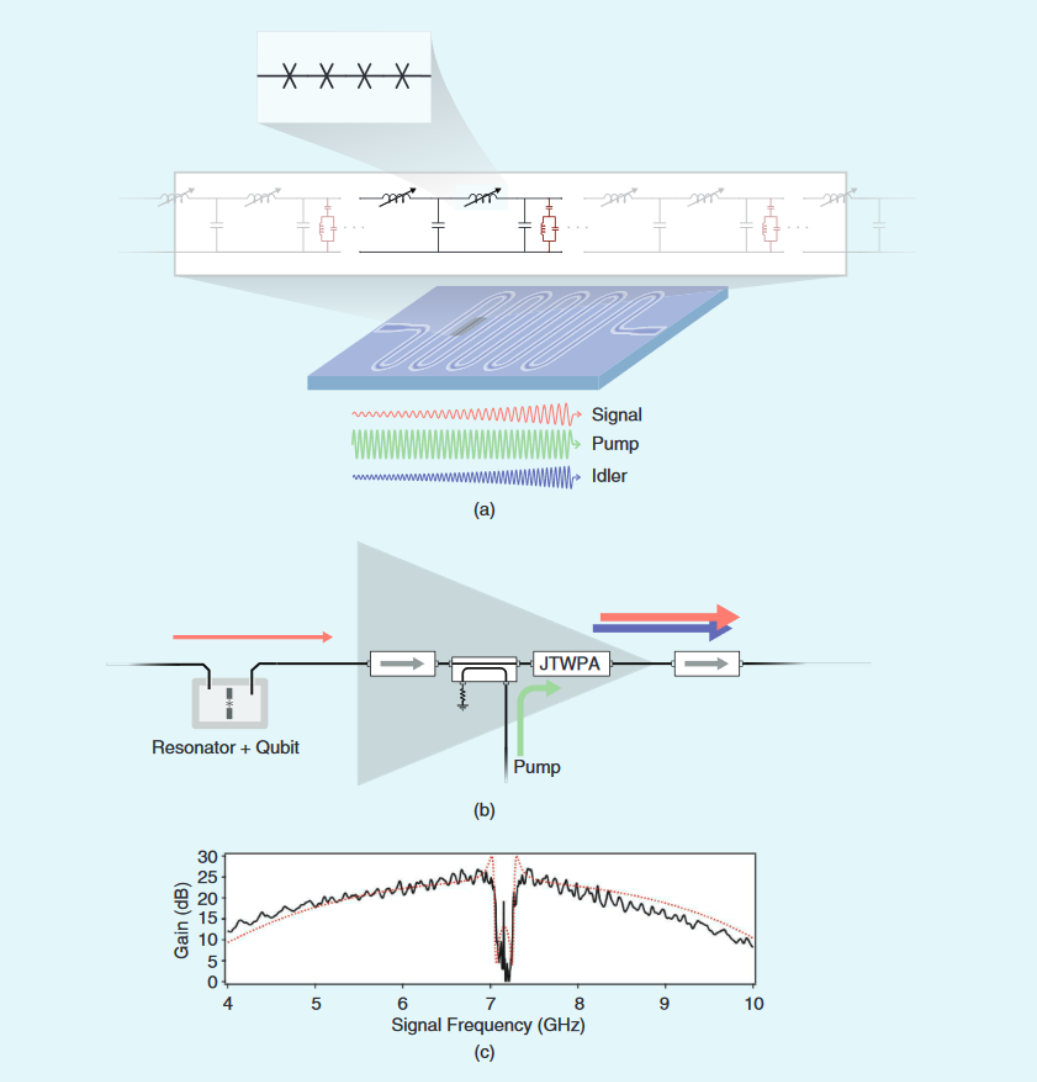

Figure 2.1: Schematic description of JTWPA(Cited from [2]).(a)The JTWPA is constructed as a 50-Ω transmission line with series Josephson junctions (b)The qubit measurement configuration, including cryogenic isolators(box with grey arrows) and a directional coupler(box with two black lines, one of which is shorted). Arrows with color denote different Microwave tones (c)Measured gain versus signal frequency, the pump frequency lies within the transmission dips. The red dots correspond to theoretical values.

$$
\begin{aligned}
G &= 10log_{10}\frac{P_{Amplified}}{P_{Not\ amplified}} \\
&= 20log_{10}\frac{|S_{21}|_{Amplified}}{|S_{21}|_{Not\ amplified}},
\end{aligned}
\tag{2.2}
$$

where $|S_{21}|$ corresponds to the scattering parameter of the signal tone. It could be understood as the measured amplitude of the output signal. Therefore it has a square relation with the power.

Bandwidth

Bandwidth describes the signal frequency range where the signal could be sufficiently amplified. In this thesis, the bandwidth is defined as the frequency range at half maximum performance, i.e. the frequency range where $G(\omega_s) > G_{max} - 3dB$ in decibels units.

Saturation power

Saturation power describes the upper limit of power under which the signal tone can be effectively amplified. Here the saturation power is defined as the power threshold under which $G(P_s) > G_{max} - 1dB$ in decibels units.

2.1.3 Noise temperature of amplifier and amplifier chain

In order to characterize the intrinsic noise of an amplifier with a bandwidth B and gain G, *noise temperature* is introduced and defined as[18]:

$$
T_e = \frac{N_o}{GkB}, \tag{2.3}
$$

where N_o is the output noise power that comes only from the intrinsic channel of the amplifier and k is Boltzmann's constant. One way to understand noise temperature is to imagine two equivalent model where a noisy amplifier connected to noiseless signal source and another noiseless amplifier connected to noisy signal source, as shown in Fig.2.2. For the noisy signal source, the noise is the *thermal noise* generated by a resistor of temperature T_e.

For a chain of cascaded amplifiers, the effective noise temperature of the whole amplifier chain can be expressed as[12]:

$$
T_{sys} = T_{N,1} + \frac{T_{N,2}}{G_1} + \frac{T_{N,3}}{G_1 G_2} + \cdots, \tag{2.4}
$$

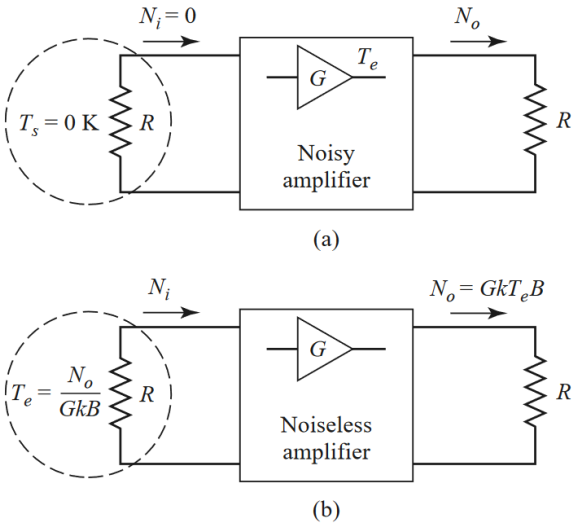

Figure 2.2: Defining the equivalent noise temperature of a noisy amplifier(Cited from [18]). The two models have the same output load power.(a)Noisy amplifier. (b)Noiseless amplifier

where $n = 1, 2, 3, ...$ denotes the order of amplifiers starting from the signal input, T and G denote the noise temperature and gain. As shown in Eq., T_{sys} is dominated by the noise contribution from the first amplifier, whereas the gain of the first amplifier has the effect of supperssing the noise from the amplifier of higher order[12].

2.1.4 Representation Microwaves in Heisenberg picture

Microwaves are electromagnetic fields and therefore considered to be coherent light comprising microwave photons[12]. In Heisenberg picture, the microwave field could be represented as an operator $\hat{a}$ with commutation relation[12, 19, 20, 21]:

$$[\hat{a}, \hat{a}^\dagger] = 1 \tag{2.5}$$

2.1.5 Quantum-limited amplifier

Core message: For phase-insensitive amplifier, the minimum noise allowed by quantum mechanics is half quanta.

Quantum mechanics uses operators to describe the process of signal amplification. For a phase-insensitive amplifier, the amplified signal could be expressed as[21, 22]:

$$\hat{a}_{amp} = \sqrt{G}\hat{a}_{in} + \sqrt{G-1}\hat{h}^{\dagger}, \tag{2.6}$$

where G is the power gain, $\hat{a}_{in}$ represents the input field, and $\hat{h}^{\dagger}$ accounts for noise added by amplifier. This input-output relation could be cast in another form:

$$\langle|\hat{a}_{amp}|^2\rangle = G(\mathcal{A} + \langle|\hat{a}_{in}|^2\rangle). \tag{2.7}$$

Here $\langle|\hat{O}|^2\rangle = \langle\{\hat{O}^{\dagger}, \hat{O}\}\rangle/2$ is the symmetrized fluctuations. According Caves' theorem, the noise added by amplifier is[21]

$$\mathcal{A} = \frac{(G-1)}{G}\left(\langle\hat{h}^{\dagger}\hat{h}\rangle + \frac{1}{2}\right). \tag{2.8}$$

In the limit of low amplifier noise $\langle\hat{h}^{\dagger}\hat{h}\rangle \to 0$ and large gain, this added noise is found to be bounded by $\mathcal{A} \geq 1/2$, corresponding to half a photon of noise. Therefore, quantum mechanics throw a lower limit on the noise added by amplifier during signal amplification, and a amplifier that reaches this limit is referred as quantum-limited amplifier.

2.1.6 Quantum efficiency of a quantum-limited amplifier

Quantum efficiency η can be used to characterize the performance of a quantum-limited amplifier, as shown in Fig.2.3. It is defined by modeling the noisy amplifier with a noiseless amplifier of gain $G/\bar{\eta}$ preceded by a beam splitter of transmittivity $\bar{\eta}$. To avoid the violation of commutation relation in Eq.2.5, vacuum noise $\hat{v}$ is added in the beam splitter. The input-output relation of this noiseless amplifier reads $\hat{a}_{amp} = \sqrt{G/\eta}(\sqrt{\eta}\hat{a}_{in} + \sqrt{1-\eta}\hat{v})$. Similar to Eq.2.7, the output noise of this noiseless amplifier could be expressed as:

$$\langle|\hat{a}_{amp}|^2\rangle = \frac{G}{\eta}\left[(1-\eta)\frac{1}{2} + \eta\langle|\hat{a}_{in}|^2\rangle\right]. \tag{2.9}$$

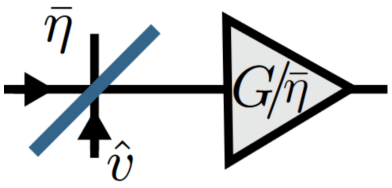

Figure 2.3: Modeling a noisy amplifier with a noiseless amplifier preceded by a beam splitter(Cited from [23])

Comparing it to Eq.2.7 and Eq.2.8, we arrive at

$$\eta = 1/(2\mathcal{A} + 1) \leq 1/2 \tag{2.10}$$

Importantly, the concept of quantum efficiency is not limited to amplification, and can be applied to the whole chain that consists of all kinds of electronic components[23].

2.2 Transmon Qubit

2.2.1 Circuit Hamiltonian for Transmon Qubit

Here, we discuss the circuit Hamiltonian for the transmon qubit coupled to a resonator to understand its importance for the extraction of quantum efficiency of qubit readout system. For this coupled system, the Hamiltonian can be written as [23]:

$$\hat{H} = 4E_C \left(\hat{n} + \hat{n}_r\right)^2 - E_J \cos\hat{\varphi} + \sum_m \hbar\omega_m \hat{a}_m^\dagger \hat{a}_m, \tag{2.11}$$

where $\hat{n}_r = \sum_m \hat{n}_m$ with $\hat{n}_m = (C_g/C_m)\,\hat{Q}_m/2e$ is the contribution to the charge bias due to the m-th resonator mode. C_g is the gate capacitance and C_m is the associated resonator mode capacitance.

We restrict the Hamiltonian by assuming that the transmon frequency is much closer to the fundamental resonator modes, $|\omega_0 - \omega_q| \ll |\omega_m - \omega_q|$ for $m \geq 1$, we truncate the sum over m to a single term:

$$\hat{H} = 4E_C \left(\hat{n} + \hat{n}_r\right)^2 - E_J \cos\hat{\varphi} + \hbar\omega_r \hat{a}^\dagger \hat{a} \tag{2.12}$$

In this single-mode approximation, the transmon-resonator system is equivalent to a transmon capacitively coupled to an LC resonator, as in Fig. 2.4.

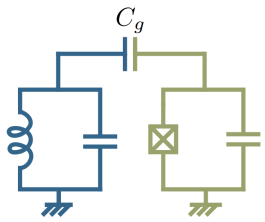

Figure 2.4: A lumped-element LC circuit representing a transmon capacitively coupled to an LC oscillator(Cited from [23]).

Now, we rewrite the charge and flux variables $\hat{\varphi}$ and $\hat{n}$ for the transmon

in terms of ladder operators $\hat{b}^\dagger$ and $\hat{b}$:

$$\hat{\varphi} = \left(\frac{2E_C}{E_J}\right)^{1/4} \left(\hat{b}^\dagger + \hat{b}\right) \tag{2.13}$$

$$\hat{n} = \frac{i}{2}\left(\frac{E_J}{2E_C}\right)^{1/4} \left(\hat{b}^\dagger - \hat{b}\right) \tag{2.14}$$

Thus, we can rewrite the transmon-resonator Hamiltonian as:

$$\hat{H} \approx \hbar\omega_r \hat{a}^\dagger\hat{a} + \hbar\omega_q \hat{b}^\dagger\hat{b} - \frac{E_C}{2}\hat{b}^\dagger\hat{b}^\dagger\hat{b}\hat{b} - \hbar g\left(\hat{b}^\dagger - \hat{b}\right)\left(\hat{a}^\dagger - \hat{a}\right), \tag{2.15}$$

where ω_r is the frequency of the resonator and

$$g = \omega_r \frac{C_g}{C_\Sigma}\left(\frac{E_J}{2E_C}\right)^{1/4}\sqrt{\frac{\pi Z_r}{R_K}}, \tag{2.16}$$

where Z_r is the characteristic impedance of the resonator mode and $R_K = h/e^2 \sim 25.8k\Omega$ is the resistance quantum.

In practice, the coupling between transmon and resonator is usually weak in comparison to the qubit transition energy, with $|g| \ll \omega_r, \omega_q$. This allows us to use a rotating-wave approximation to further simplifying the original Hamiltonian into:

$$\hat{H} \approx \hbar\omega_r \hat{a}^\dagger\hat{a} + \hbar\omega_q \hat{b}^\dagger\hat{b} - \frac{E_C}{2}\hat{b}^\dagger\hat{b}^\dagger\hat{b}\hat{b} + \hbar g\left(\hat{b}^\dagger\hat{a} + \hat{b}\hat{a}^\dagger\right). \tag{2.17}$$

2.2.2 Transmon Circuit in Dispersive Regime

For quantum information processing, it is practical to work in the dispersive regime where the qubit-resonator detuning is large with respect to the coupling strength $|g/\Delta| \ll 1$, where $\Delta = \omega_q - \omega_r$ is the qubit-resonator detuning [23]. In this regime, qubit and resonator are only weakly entangled and a simplified model can be obtained from second-order perturbation theory. Using Schrieffer-Wolff perturbation theory [23] and truncating Eq. (2.17) to the first two levels of the transmon, we obtain:

$$\hat{H}_{disp} \approx \hbar\omega_r' \hat{a}^\dagger\hat{a} + \frac{\hbar\omega_q'}{2}\hat{\sigma}_z + \hbar\chi\hat{a}^\dagger\hat{a}\hat{\sigma}_z, \tag{2.18}$$

with the dressed frequencies and the qubit-state-dependent dispersive cavity shift:

$$\omega_r' = \omega_r - \frac{g^2}{\Delta - E_C/\hbar} \tag{2.19}$$

$$\omega_q' = \omega_q + \frac{g^2}{\Delta} \tag{2.20}$$

$$\chi = -\frac{g^2 E_C/\hbar}{\Delta\left(\Delta - E_C/\hbar\right)} \tag{2.21}$$

It is noteworthy that this approximation is valid only when the average resonator photon number is way below the critical value: $\bar{n} \ll (\Delta/2g)^2 = n_{crit}$. In practice this criteria is usually written as $\bar{n}/n_{crit} < 0.1$ [23]. If we set $\Delta = 2\pi \times 2GHz$ and $g = 2\pi \times 200MHz$, the critical photon value should equal to 25, which means that the average photon number should be below 2.5.

It is instructive to rewrite Eq. (2.21) as to emphasise the frequency shifts that appear in the experiment:

$$\hat{H}_{\text{disp}} \approx \hbar\omega_r \hat{a}^\dagger \hat{a} + \frac{\hbar}{2}\left[\omega_q + 2\chi\left(\hat{a}^\dagger \hat{a} + \frac{1}{2}\right)\right]\hat{\sigma}_z. \tag{2.22}$$

The cavity frequency is pulled by this interaction with the qubit and reads $\omega_r \pm \chi$ depending on the qubit state. In the dispersive regime, the g-e transition frequency of the qubit in the absence of resonator photons is Lamb shifted and takes the value $\omega_q + \chi$. An increase in the photon population leads to a qubit-frequency shift, so called ac start shift, by an average value of $\Delta\omega_q = 2\chi\left\langle \hat{a}^\dagger \hat{a}\right\rangle$. Given the dependence of the qubit frequency on the measurement power, knowing the value of χ will allow us to infer the intracavity photon number as a function of input power at the cavity frequency [24].

2.2.3 Resonator spectroscopy and qubit spectroscopy

Core message: Both resonator spectroscopy and qubit spectroscopy are repeated with different powers until the resonance is found.

Spectroscopy generally refers to the measurement of intensity as a function of frequency and is commonly used in cQED experiments to determine resonance frequencies of resonators and qubits[1].

To begin with, a single-tone spectroscopy is performed to identify the frequency of the readout resonator. In the case of several $\lambda/4$ CPW(coplanar waveguide) resonators capacitively coupled to a common microwave feedline, the measured scattering parameter S_{21} of each resonator in response to a readout tone at $\omega = 2\pi f$ is described by a Lorentzian line shape[1, 25]:

$$S_{21} = A\left[1 + \alpha\frac{\omega - \omega_r}{\omega_r}\right]\left[1 - \frac{|\kappa_c|/\kappa}{1 + 2i\frac{\omega-\omega_r}{\kappa}}\right]e^{i(\tau\omega+\phi_0)}, \tag{2.23}$$

where A is the transmission amplitude away from resonance, ω_r is the qubit-state-dependent resonance frequency of the readout mode, α allows a linear variation in the overall transmission chain in the narrow frequency range around any given resonance, τ and ϕ_0 relate to propagation delays to and from the sample, κ_c and κ are frequency independent coupling rate determined by system configuration.

This model also includes a number of non-ideal elements, including both inductive and capacitive coupling, and impedance mismatch in the feedline[25]. As seen from Fig.2.5(b), for a hanger configuration, the resonance corresponds to a dip in the measured $|S_{21}|$, and a clear asymmetry in the line shape is also observed, which is due to the coupling line mismatch[26].

It is important to note that this one-tone spectroscopy experiment takes place before the optimization of the various pulses and amplification configurations. Thus, it can be challenging to obtain a clean signal at this stage[1]. A useful technique to address this issue is to repeatedly perform one-tone spectroscopy at different power level. In the high-power limit, the resonator could be driven to a "bright" state regardless the state of the qubit[27], where the bare resonance frequency of the readout mode ω_R could be located[1]. On the other hand, the resonance will undergo a clear shift as the power is progressively reduced to the few photon limit, where a qubit is dispersively coupled to the resonator[1]. This power-dependent frequency shift is the Lamb shift $\Lambda_\chi = g^2/\Delta$. In this sense, this power sweep provides a convenient test of whether the resonator is coupled to a qubit mode[1].

Based on this power-versus-frequency sweep, we can now choose an appropriate readout power for the subsequent characterization experiments[1]. It should be low enough that the qubit is dispersively coupled to the resonator. Meanwhile, it should be high enough to produce a sufficiently high signal for detection.

After targeting the resonator frequency, qubit frequency could also be targeted using a technique referred as "two-tone" continuous-wave spec-

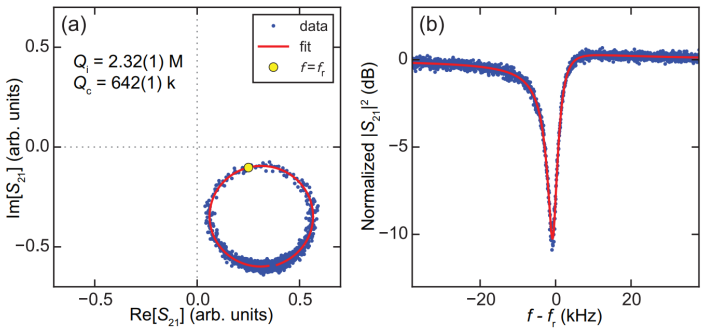

Figure 2.5: Typical measured response of a CPW resonator around its resonance frequency(Cited from [25]). (a) Trajectory of S_{21} in the complex plane with a fit. (b) Normalized $|S_21|$ calculated from (a)

troscopy[1]. In this protocol, a constant drive tone is applied on resonance with the resonant ω_r while a second drive ω_s with variable frequency is employed to probe the state of the qubit. While the second tone is near resonance with the qubit, it will induce a state transition of the qubit, which will in turn change the frequency of the resonator through dispersive coupling. As a result, the response of the resonator to the constant drive tone will be reverted.

2.2.4 Nanowire transmon and the gate tunability

Core message: Nanowire Transmon's Josephson junction is made of nanowire with a gate beneath it. Tuning the gate could change Transmon's qubit frequency.

Core message2: Performing a resonator spectroscopy in the low-power regime while tuning the gate could help us find the sweet spot for qubit. The qubit is at the sweet spot when resonator frequency is at a maximum.

Nanowire-transmon is a transmon whose Josephson junction is made of a semiconductor nanowire with an controlling electrostatic gate. In contrast to a flux-tunable Transmon, e.g., SQUID qubit[28], Josephson energy of nanowire-transmon is controlled the electrostatic gate. As a result, the qubit frequency could be tuned by tuning the biasing voltage of the gate[29].

While it is convenient to tune qubit frequency through gate biasing, the qubit is could be subject to charge dispersion, as shown in Fig.2.6.

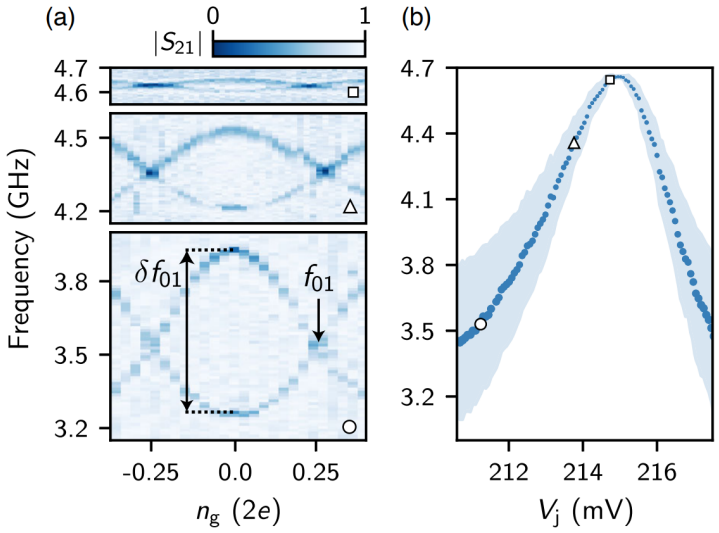

Figure 2.6: Evolution of the qubit frequency and charge dispersion as a function of gate voltage V_j(Cited from [30]) (a) Qubit frequency versus offset charge tuned by V_j (b) Extracted f_{01}(markers) and δf_{01} (shading and marker size versus V_j). Open markers indicate the positions of (a)

2.2.5 Rabi experiment and X gate

In Rabi experiments, qubit state oscillates between $|0\rangle$ and $|1\rangle$ as a function of the external "impulse", i.e., the time integral of the applied pulse amplitude[1]. Rabi experiments could done by applying a pulse at the qubit frequency with a fixed duration and varying its amplitude, also referred as "Amplitude Rabi". From the resulting oscillations, the amplitude required to flip qubit state between $|0\rangle$ and $|1\rangle$ could be determined[1]. The resulting pulse is referred as pi pulse.

To be more general, for a coherent drive of time-dependent amplitude $\epsilon(t)$, frequency ω_d and phase ϕ_d on a transmon could be modeled by[23]:

$$\hat{H} = \frac{\hbar\delta_q}{2}\hat{\sigma}_z + \hbar\epsilon(t)[\cos(\phi_d)\hat{\sigma}_x + \sin(\phi_d)\hat{\sigma}_y], \tag{2.24}$$

where $\delta_q = \omega_q - \omega_d$ is the detuning between the qubit and the drive frequencies, $\hat{\sigma}_z$ denotes the truncated two-level transmon qubit system, $\hat{\sigma}_x$ and $\hat{\sigma}_y$ represent the π rotation along X-axis and Y-axis in the Bloch sphere. As described in the Hamiltonian, the phase of the drive ϕ_d controls the axis of

rotation. In other words, any axis of rotation in the $X-Y$ plane could be achieved by tuning ϕ_d.

2.2.6 Relaxation time and dephasing time

Relaxation time T_1 and dephasing time T_2 describes the coherence properties of the qubit. Here we introduce the experiment used to measure T_1 and T_2.

To measure the relaxation time T_1, qubit is repeatedly prepared in excited state and then measured the state after a variable interval time t. This results in an exponentially decaying signal, given by[1]

$$S(t) = A \times e^{-t/T_1} + B, \tag{2.25}$$

where $S(t)$ is the signal as a function of wait time t, A and B are scaling and offset factors.

The Ramsey dephasing time T_2 can be obtained by initializing the qubit in $|0\rangle$, applying a pi/2 pulse, waiting for a time t, applying a final pi/2 pulse and then measuring the qubit. This will produce an (often exponentially) decaying oscillation described by[1]:

$$S(t) = Ae^{-(t/T_2)^n} \times [\cos(\omega t + \phi) + C] + B, \tag{2.26}$$

where A, B,and C are scaling and offset factors, n describes the profile of the exponential decay, and ω the angular frequency of the oscillation.

The profile of the decay n in Eq.2.26 provides some indication of the limiting mechanism of T_2. If T_2 is limited by T_1 or another source of incoherent noise, $n \approx 1$. If there is a coherent noise process, such as a slow drift in the qubit frequency, n will be larger than 1[1].

The oscillation frequency ω corresponds to the frequency detuning between the pi/2 pulse and the actual qubit frequency. In practice this frequency can be increased by tuning the phase of the second pi/2 pulse (artificial detuning)[1].

The Ramsey time contains information on both energy relaxation and pure dephasing(T_ϕ) in the qubit, i.e., $1/T_2 = 1/(2T_1) + 1/T_\phi$[1]. It quantifies the effective decoherence timescales of the qubit.

2.2.7 Fine coherence experiment

In order to measure qubit's coherence after certain amount of dephasing, an experiment similar to T_2 measurement could be applied. As shown in Fig.2.7,

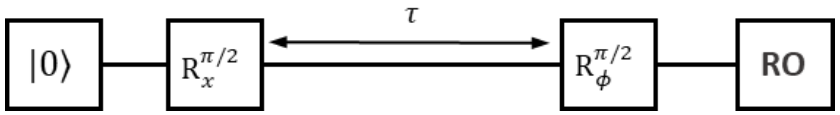

Figure 2.7: Coherence measurement. The second $pi/2$ pulse has a variable phase φ

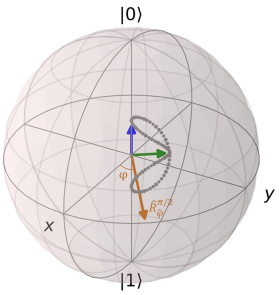

Figure 2.8: Bloch-sphere visualization of qubit state and the rotation of which. The green arrow denotes the original qubit state. The brown arrow denotes the rotation vector. The grey dots denote the possible final state for different rotation axis. We see that the projection of the final state would have a maximum value(blue arrow) when the rotation axis is perpendicular to initial arrow.

by sweeping the phase of the second $pi/2$ pulse of the Ramsey sequence, the remaining of the coherence of qubit after a fixed amount of dephasing time could be measured.

To understand this process, consider a random qubit state in the X-Y plane of the Bloch sphere. By sweeping the rotation axis of the second $\pi/2$ pulse and then projecting the state into computational basis, an oscillation of expected value could be observed. The amplitude of this oscillation corresponds to the coherence of qubit. According to Eq.2.24, the rotation axis orientation in the Bloch sphere could be changed by tuning the phase of the second drive pulse.

2.2.8 Source of noise

Introduced here were four kinds of stochastic noise. They arise from random fluctuations of parameters that are coupled to the qubit[12].

Charge noise

Charge noise arises from charged fluctuators present in the defects or charge traps that reside in solid-state devices[12]. It is usually modeled as an ensemble of fluctuating two-level systems or as bulk dielectric loss[31, 32].

In the case of a transmon qubit, this noise is mainly responsible energy relaxation(T_1). However, if the E_J/E_C ratio is not sufficiently large(smaller than 60), the qubit frequency itself will also be sensitive to broadband charge fluctuations. In this case, charge noise also causes pure dephasing(T_ϕ)[12]. This effect could be modeled by the transmon Hamiltonian:

$$\hat{H} = 4E_C(\hat{n} - n_g)^2 - E_J \cos(\hat{\varphi}), \tag{2.27}$$

where $\hat{n} = \hat{Q}/2e$ is the charge number operator, n_g is the possible offset charge that describes charge noise, ϕ is the phase operator, E_C and E_J are the charging energy and Josephson energy.

From this Hamiltonian we see that the energy spectrum of transmon depends on the offset charge n_g. In fact, this dependence decrease with regards to the increase of ratio E_J/E_C, as shown in Fig.2.9.

Photon number fluctuations

In the circuit QED architecture, resonator photon number fluctuation is another major decoherence source147[12, 24]. Photon-number fluctuations of the residual microwave fields in the cavity could also lead to a qubit frequency shift $\Delta_{Stark} = 2\eta\chi\bar{n}$, where $\bar{n}$ is the average photon number inside the cavity, and η is a scaling coefficient decided by χ and resonator decay rate κ.

Quasiparticles

Another important noise source for superconducting devices are *Quasiparticles*, i.e., unpaired electrons[12]. They are naturally excited due to thermodynamics, and the quasiparticle density in equilibrium superconductors should be exponentially suppressed as temperature decreases. However, this

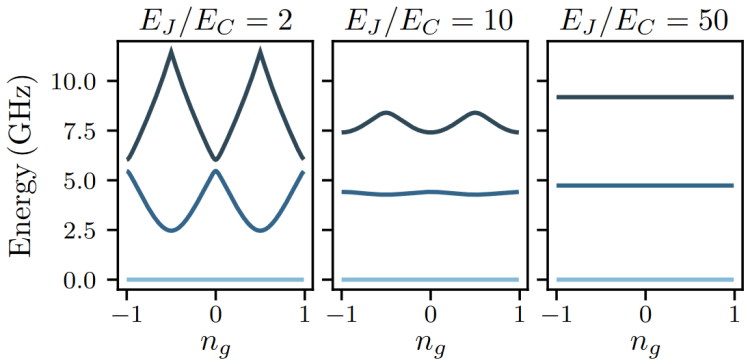

Figure 2.9: Frequency difference $\omega_j - \omega_0$ for the first three energy levels of the transmon Hamiltonian obtained from numerical diagonalization of Eq.2.27. Qubit frequency was set to 5GHz.(Cited from [23])

is not the case below about 150 mK, where the quasiparticle population is much higher than expected due to unknown reasons[12].

The tunneling of quasiparticles through a qubit junction may lead to both T_1 relaxation and pure dephasing T_ϕ, depending on the type of qubit, the bias point, and the junction through which the tunneling event occurs [12, 33, 34]

2.3 Readout of superconducting qubits

2.3.1 Microwave detection and qubit state

In the dispersive regime, the transmon-resonator Hamiltonian is approximated by:

$$\hat{H}_{disp} \approx \hbar \left(\omega_r + \chi \hat{\sigma}_z\right) \hat{a}^\dagger \hat{a} + \frac{\hbar \omega_q}{2} \hat{\sigma}_z \tag{2.28}$$

As seen in the Hamiltonian, the resonator frequency becomes qubit-state dependent in the dispersive regime. As a result, the internal field $\alpha(t)$ of the resonator, which is usually referred as the intra-cavity field, becomes qubit state dependent.

In fact, the internal field of the resonator is determined by the qubit state

and the pulse that was driving the resonator:

$$\dot{a}_{|0\rangle/|1\rangle} = -i\epsilon f(t) - i\left(\delta \pm \chi\right)\alpha(t) - \frac{\kappa}{2}\alpha(t), \tag{2.29}$$

where $\epsilon f(t)$ is the envelope of the pulse, and Δ the detuning of it from the resonator frequency. In this situation, driving the cavity results in a qubit-state dependent coherent state $|\alpha_{0/1}$. In addition, if qubit is in a superposition state, the system would evolve to an entangled qubit-resonator state of the form[23]:

$$c_0|0, \alpha_0\rangle + c_1|1, \alpha_1\rangle. \tag{2.30}$$

In conclusion, we could read out the qubit state by inputting a readout pulse and then measuring the scattered output, which will be denoted as the signal for further discussion.

2.3.2 Qubit measurement chain

Core message: A typical chain is made up of quantum-limited amplifier, HEMT, IQ mixer.

In the architecture of circuit QED, superconducting qubit state is measured by measuring scattering of a microwave probe tone off an oscillator coupled to the qubit[23]. Because of the small energy of microwave photons with respect to the room temperature thermal radiation, measurements in circuit QED rely on amplification of weak microwave signals followed by detection of field quadratures using heterodyne detection[23].

A typical measurement chain in circuit QED is illustrated in Figure 2.10[23]. The signal (RF) from a microwave source is applied to the input port of the resonator. Then the resonator's output field is first amplified by a quantum-limited amplifier, a amplifier whose internal noise reaches the limit allowed by quantum mechanics, and then by an HEMT amplifier. After amplification, the amplified microwave signal is down-converted into two lower Intermediate-frequency(IF) signals. These two IF signals are referred as the two quadrature components the original signal. Therefore they are denoted as I(In-phase) signal and Q(Quadrature) signal. The two signals are then digitized and processed by an analog-to-digital converter (ADC) and field-programmable gate array (FPGA).

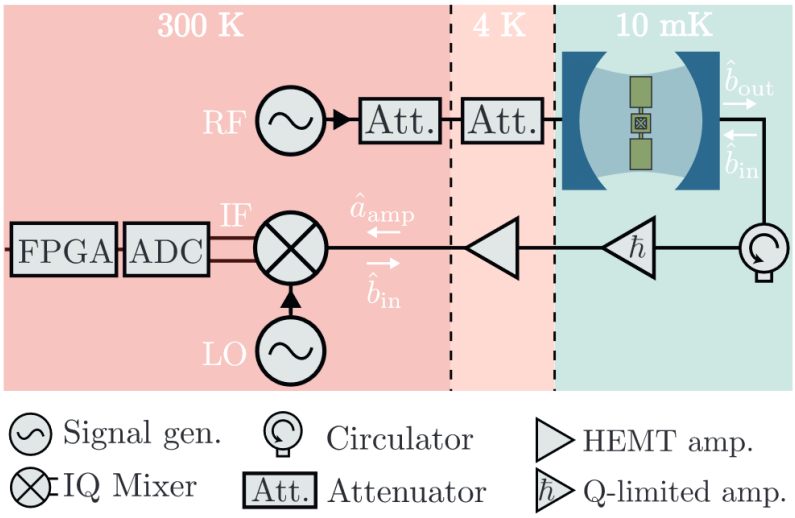

Figure 2.10: Schematic representation of the microwave measurement chain for field detection in circuit QED, with the resonator depicted as a Fabry-Perot cavity(Cited from [23]). Here the signal of interest is denoted as $\hat{a}_{amp}$, whereas $\hat{b}_in$ denotes the input field moving towards the transmon chip in the opposite direction to the signal $\hat{a}_{amp}$

2.3.3 Quantum efficiency of measurement chain

In a circuit QED measurement, the maximum information acquired, given by the SNR, is equal to the amount of qubit information destroyed, given by the total dephasing $\gamma_\varphi = \int_0^\tau \Gamma_\varphi(t)dt$ (up to a numerical factor)[1]. Here Γ_φ is referred to as the measurement-induced dephasing rate, and τ denotes the total measurement time. In practice, signal suffers from degradation due to either photon loss or added noise as it travels to the acquisition system at room temperature. The resulting SNR will therefore be lower compared to its theoretical maximum. This nonideality is quantified by the *quantum efficiency* η given by[1]

$$\eta = \frac{SNR^2}{4\gamma_\varphi}. \tag{2.31}$$

On the other hand, *quantum efficiency* is related with the *noise temperature* by[12, 15]

$$\eta = \frac{\hbar\omega_s}{k_b T_{sys}}, \tag{2.32}$$

where ω_r denotes the frequency of the signal, k_b the Boltzmann's constant, and T_{sys} the *noise temperature* of the whole readout chain.

As discussed in Eq.2.1.3, implementing a quantum-limited amplifier as the first amplifier of the amplifier chain can reduce the *noise temperature* of the system and hence increase the *quantum efficiency*. For state-of-art circuit QED setups, the quantum efficiency is reported to be between 0.1 and 0.6[35, 36, 37, 38, 39].

Notice that the definition of *quantum efficiency* of the whole measurement chain is consistent with that of a single amplifier, as mentioned in Subsec.2.1.6. In fact, the *quantum efficiency* of the measurement chain could be decomposed into the product of the *quantum efficiency* of every individual components[14, 15].

2.3.4 IQ detection

Core message: The amplified signal is down-converted and decomposed into I signal and Q signal.

A readout event commences with a short microwave tone directed to the resonator at the resonator probe frequency ω_{RO}. After interacting with the resonator, the scattered microwave signal would carry the resonator signature, i.e. the qubit-state-dependent amplitude and phase. Therefore, the

goal is to best distinguish the classical resonator signatures corresponding to our qubit states[12].

To gain intuition, we could use phasor $A_{RO}\exp(j\theta_{RO}) \equiv A_{RO}\angle\theta_{RO}$ to specify a harmonic signal $s(t)$ at a known frequency ω_{RO}[12]. Here A_{RO} and θ_{RO} are respectively the signal amplitude and phase that could be used to read out the qubit states. To perform qubit readout, the goal is to measure the "in-phase" component I and a "quadrature" component Q of the complex number represented by the phasor,

$$A_{RO}e^{j\theta_{RO}} \equiv I + jQ, \tag{2.33}$$

to determine A_{RO} and θ_{RO} (or their scaled and offset versions)[12].

One direct means to extract I and Q is to perform a heterodyne measurement using an analog IQ mixer. As illustrated in Figure 2.11(a), the local oscillator and readout tone are detuned such that $\omega_{IF} = |\omega_{RO} - \omega_{LO}| > 0$, usually in the range of few tens to a few hundreds of MHz[23]. They are then mixed in the IQ mixer, yielding $I_{IF}(t)$ quadrature and $Q_{IF}(t)$ quadrature at a down-converted intermediate frequency ω_{IF}. The intermediate frequency is now low enough such that $I_{IF}(t)$ and $Q_{IF}(t)$ could be digitized using commonly available analog-to-digital converters (ADCs)[12].

As shown in Figure 2.11(b), pulsing the resonator is necessarily accompanied by a ring-up time, which is related to the quality factor of the resonator. This results in an increase and decrease of the amplitude of the field that passes through ADCs at the beginning and end of the measurement. The field at these two stage is expected to reveal low signal while having the same noise as the middle plateau due to the internal dynamics of the readout resonator.[1, 14, 40]. Therefore, to avoid sampling the resonator transient, some readout delay (τ_{rd}) corresponding to the resonator linewidth will be added, and IQ quadratures are sampled for a time window of length τ_s, where both quadratures are stable[12].

Figure 2.11(c) visualizes the workflow of how the sampled IQ quadratures are together demodulated into a single point in the complex $I - Q$ plane. In the first step, sampled IQ quadratures $I_{IF}[n]$ and $Q_{IF}[n]$ are assembled into a single function z_{IF}:

$$z_{IF}[n] = I_{IF}[n] + jQ_{IF}[n] \equiv V_I[n] + jV_Q[n], \tag{2.34}$$

where the digital in-phase and quadrature signals are represented here as the voltages $V_I[n]$ and $V_Q[n]$ sampled by the ADC, as shown in Figure 2.11(b).

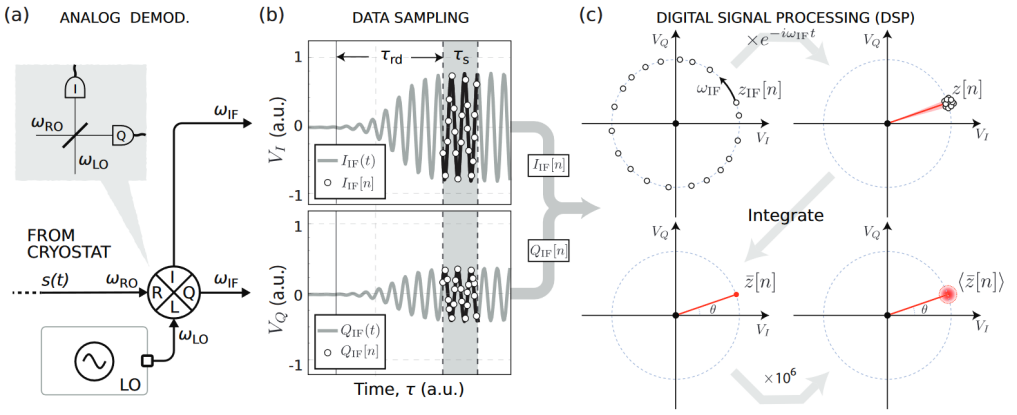

Figure 2.11: Schematic of the heterodyne detection technique(Cited from [12]).

As seen in the first step of the demodulation workflow, $z_{IF}[n]$ is a time series that is rotating around the origin with an oscillatory exponential $e^{j\Omega_{IF}n}$, where $\Omega_{IF} = \omega_{IF}\Delta t$ is the digital frequency, and Δt is the sampling period.

In the second step, z_{IF} is point-by-point multiplied by the complex conjugate of the oscillatory exponential:

$$z[n] = z_{IF}[n].* e^{-j\Omega_{IF}n}. \tag{2.35}$$

For every sample point of z_{IF}, this multiplication will result in a phasor denoted in a point in the $I - Q$ plane. As a result we obtained an assemble of phasor with a small amount of deviation.

For the third step, this assemble of phasor is averaged into one single phasor $\bar{z}$, which could be used to find A_{RO} and θ_{RO} of interest. For the fourth step, the "single-shot measurement" described in the previous three is repeated a large number of times to obtain an ensemble average $\langle\bar{z}\rangle$. Meanwhile, the statics of single-shot measurement result $\bar{z}$ can be used to analyze the readout performance of the system, i.e. single-shot readout fidelity and SNR.

2.3.5 Q function and qubit state signal distribution

Here we aimed at explaining why qubit sate signal distribution is expected to follow a Gaussian distribution.

In the context of field detection, it is particularly useful to represent the quantum state of the electromagnetic field using phase-space representations. One of such is the Husimi-Q representation:

$$Q_\rho(\alpha) = \frac{1}{\pi}\langle\alpha|\rho|\alpha\rangle, \tag{2.36}$$

where ρ is the state of the electromagnetic field and $|\alpha\rangle$ is one of the eigenstate of the intra-cavity field $\hat{a}$ in the Heisenberg picture. This function represents the probability distribution of finding ρ in the coherent state $|\alpha\rangle$. Here α is a complex number with $\alpha = x + jp$, where x and p defined as the dimensionless position and momentum coordinate of the phase space.

If the cavity is in a coherent state $|\beta\rangle$, then the Q-function takes the form[23]:

$$Q_{|\beta\rangle}(\alpha) = W_{|\beta\rangle}(\alpha) * W_{|0\rangle}(\alpha), \tag{2.37}$$

where $W_{|\beta\rangle}(\alpha) = \frac{2}{\pi}e^{-2|\alpha-\beta|^2}$ is a Gaussian centered at β in phase space and $W_{|0\rangle}(\alpha)$ is also a Gaussian that describes quantum fluctuation of vacuum state.

According to Caves et al.[41], the probability distributions for the simultaneous measurement of two orthogonal quadratures in heterodyne detection is given by the marginals of the Husimi-Q distribution. In other words, the probability distribution for the 'single-shot measurement' $\bar{z}$ described above is expected to be characterized by the marginal of the Q-function of the intra-cavity field. If the resonator is driven by a coherent readout pulse, then $\bar{z}$ is expected to be Gaussian distributed in the $I-Q$ plane due to both classical and quantum noise[23, 12, 1], where the quantum noise part is shown in Eq.2.37.

2.3.6 State discrimination, square weights and optimal weights

Core message: To discriminate qubit state, I signal and Q signal are integrated together. During the integration, two kinds of weights were implemented.

Subsection 2.3.5 focuses on measuring the steady-state heterodyne signal by adding a readout delay τ_{rd} as shown in Figure2.11(b). Meanwhile, it described the process of demodulation as combining I quadrature and Q quadrature signal into a complex complex analytic function, then rotating

and averaging such function. While it could be easy to understanding and intuitively straight forward to perform such measurement, it undermines the potential to perform a fast qubit readout.

In practice, for the sake of fast qubit state discrimination, the I/Q quadratures are each multiplied with a weight function and then together integrated into a single value over the measurement window of duration T:

$$V_{int,|i\rangle} = \int_0^T \omega_I V_{I,|i\rangle} + \omega_Q V_{Q,|i\rangle} dt, \tag{2.38}$$

where this single integrated voltage value is used to discriminate qubit state directly. Therefore it is denoted with subscript $|i\rangle$ that corresponds to the qubit states $|0\rangle$ and $|1\rangle$. Here the weight function is chosen to increase the difference between ground state signal and excited state signal $\langle |V_{I,|0\rangle}\rangle - \langle V_{I,|1\rangle}\rangle|$.

It has been shown that the optimal weight function is given by the difference between the average signals corresponding to the two-qubit states[42, 43, 14]:

$$\omega_{I/Q} = \langle V_{I/Q,|1\rangle} - V_{I/Q,|0\rangle}\rangle. \tag{2.39}$$

As an alternative to optimal weight functions, often constant weight(or square weight) functions are used[14]:

$$\omega_I = \cos\varphi_\omega, \omega_Q = \sin\varphi_\omega. \tag{2.40}$$

This weight function could be imagined as rotating the signal distribution $\langle \bar{z}_{|0\rangle}\rangle$ and $\langle \bar{z}_{|1\rangle}\rangle$ in the $I-Q$ plane and use only the I component for state discrimination. Therefore, the demodulation phase φ_ω is usually chosen as to maximize the difference of the I quadrature: $\langle |V_{I,|0\rangle}\rangle - \langle V_{I,|1\rangle}\rangle|$. Then there is no information on the qubit state in the Q quadrature. Reflecting this, using only the I quadrature for discrimination could prevent the noise in Q quadrature from being integrated[23].

2.3.7 SNR and fidelity

Core message: From the integrated value distribution we get to extract the SNR and fidelity, where SNR has the strict relation if the signal distribution is real Gaussian.

As explained in subsection 2.3.4, single-shot measurement result $\bar{z}_{|0\rangle/|1\rangle}$ follows a Gaussian distribution in the I-Q plane, and the center of the Gaussian depends on the state of the qubit[35]. When the separation between the Gaussian centers('signal') is larger than their width("noise"), the qubit state could be measured with sufficient confidence. Therefore, *SNR* is defined to characterize the readout performance:

$$SNR^2 \equiv \frac{|\langle V_{int}\rangle_{|0\rangle} - \langle V_{int}\rangle_{|1\rangle}|^2}{\langle N_{int}^2\rangle_{|0\rangle} + \langle N_{int}^2\rangle_{|1\rangle}}. \tag{2.41}$$

Here $\langle V_{int}\rangle_\sigma$ is the average integrated heterodyne signal given that the qubit is in state σ, and $N_{int} = V_{int} - \langle V_{int}\rangle$ the noise operator which takes into account the system-added noise as well as the intrinsic vacuum noise of the quantum states[23].

Another figure of merit used to characterize the performance of a readout configuration is the measurement fidelity, which is defined by the measurement error[44, 43]:

$$F_m = 1 - [P(g|e) + P(e|g)], \tag{2.42}$$

where g/e represents the
ground/excited state, and $P(\sigma'|\sigma)$ denotes the empirical conditional probability of measuring state σ' when qubit was originally prepared in state σ. When single-shot measurement results strictly follow a Gaussian distribution, the measurement *fidelity* can be related with *SNR* by

$$F_m = 1 - \mathrm{erfc}(SNR), \tag{2.43}$$

where erfc is the complementary error function[44].

However, in practice, qubit relaxation and higher-order effects omitted in the dispersive Hamiltonian2.18 can lead to distortion of the coherent states and therefore to non-Gaussian marginals[23, 44]. Therefore, by measuring fidelity and SNR independently and comparing them using Eq.2.43, this equation could be used to check if the qubit stays in the dispersive regime.

2.3.8 Projection error and double-Gaussian model

Core message: One reason the distribution is non-Gaussian is due to projection error. In this case, a double-Gaussian is needed.

In practice, unwanted state transitions will happen during the process of measurement. Those transitions could be due to natural relaxation time

of the qubit, as well as induced state transitions due to a strong drive[45, 46, 47]. One direct result of those unwanted state transitions is that single-shot measurement result $\bar{z}_{|0\rangle/|1\rangle}$ no longer obey Gaussian distribution but a double-Gaussian distribution[43, 14].

2.3.9 Weak measurement

Core message: Weak measurement regime is when SNR¡1, usually due to short pulse length and strength.

Generally, while performing a qubit measurement, we assume that the quantum state is projected into either computational basis $|0\rangle$ or $|1\rangle$ and the projected state could be readout with sufficient confidence($SNR > 1$). This type of measurement is referred as a "strong measurement"[12]. As opposed to a strong measurement, a weak measurement refers to those measurements whose *SNR* is smaller than one, which means that only partial information of the quantum state is revealed to the observer.

A weak measurement corresponds to a short readout pulse length with weak pulse amplitude. In the weak measurement regime, an increase in the pulse length would result in a square root increase in *SNR*[22], and an increase in the pulse strength would result in a linear increase in *SNR*[14].

2.3.10 Quantum efficiency and noise temperature

Core message: Bultink's method could extract quantum efficiency, the quantum efficiency is related with noise temperature, the noise temperature could be measured using Macklin's method.

By measuring qubit in the weak measurement regime, quantum measurement efficiency of the system could be extracted using a three-step method proposed by Bultink et al.[14]. In this method, a readout pulse sequence categorized in the weak measurement regime is implemented. While increasing the readout amplitude ϵ, the resulted *SNR* scales linearly, $SNR = a\epsilon$, and the remaining coherence of qubit state would exhibit a Gaussian decay, $|\rho_{01}(\epsilon)| = A \cdot \exp\left(-\frac{\epsilon^2}{2\sigma_m^2}\right)$. Here $|\rho_{01}|$ is the off-diagonal component of the density matrix of the qubit state. Then quantum efficiency of the system could be characterized as:

$$\eta = \frac{SNR^2}{4\gamma_\varphi} = \frac{\sigma_m^2 a^2}{2}. \tag{2.44}$$

Two conditions are required for the second equality above: 1) optimal integration functions are used to optimally extract information from both quadratures, and 2) the intra-resonator field vanishes at the beginning and end; i.e., photons should be depleted from the resonator post-measurement[14]. This can either be done by simply waiting long enough or by using active photon depletion[14].

After the extraction of quantum efficiency, the noise temperature of the system could be calculated by[15]:

$$\eta = \frac{\hbar\omega_s}{k_b T_{sys}}, \tag{2.45}$$

where N_o is the output noise power that comes only from the intrinsic channel of the amplifier and k is Boltzmann's constant. On the other hand, the noise temperature is a quantity that could be independently characterized using a sensitive thermometer[12], such as a shot-noise tunnel junction[48] or a qubit[15], as a sensor.

Chapter 3

TWPA characterization

This chapter focuses on the experiment results and the relevant discussion. It could be chunked into three sections: Basic TWPA characterization, transmon characterization and Quantum efficiency characterization of the whole readout chain. In the basic TWPA characterization, we prepared our TWPA in a suitable working configuration. By measuring the gain, bandwidth and saturation we proved that our TWPA was suitable for the further qubit experiment. The transmon characterization served as a preparation for the third section, the extraction of quantum efficiency of the qubit readout chain. In the transmon characterization, we performed a series of basics characterization experiments about transmon. Finally, in the quantum efficiency characterization, we characterized the performance of the qubit readout chain by extracting the quantum efficiency of it.

The measurement circuit is shown in Fig.3.1. Here we used VNA to generate and analyze continuous microwave in all basic TWPA characterization experiment and partially transmon measurements. We also used OPX, a versatile qubit measurement machine, to generate and analyze microwave pulses.

3.1 Basic TWPA characterization

Using VNA(Vector Network Analyzer) to generate and analyse continuous microwave, we characterized the basic properties of amplifier. The workflow is illustrated as Fig.3.2. Firstly, we chose a signal tone with power and frequency close to the readout resonator of the transmon qubit, that we will

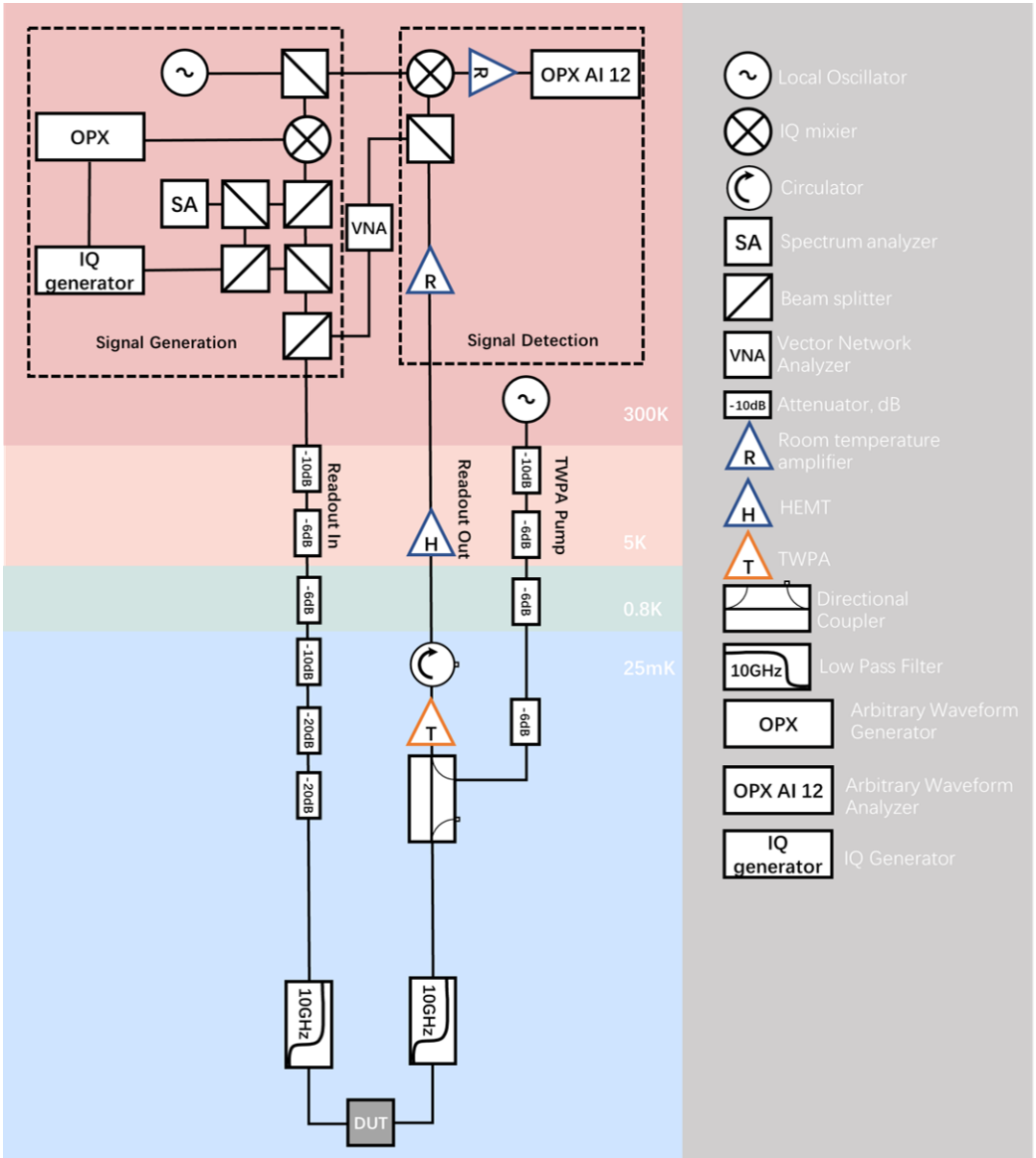

Figure 3.1: Diagram of measurement configuration

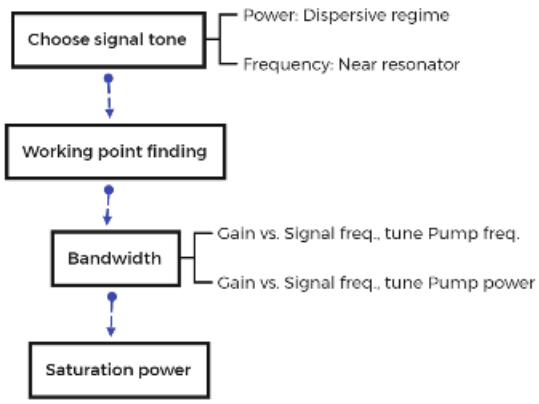

Figure 3.2: Workflow of basic TWPA characterization. The flow is chunked by 4 steps.

study later. Secondly, we find a the pump tone for maximal gain. We call this setting the working point for a given signal tone. Thirdly, we sweep the signal frequency to find TWPA's bandwidth. Fourthly, we sweep the signal power to find TWPA's saturation power.

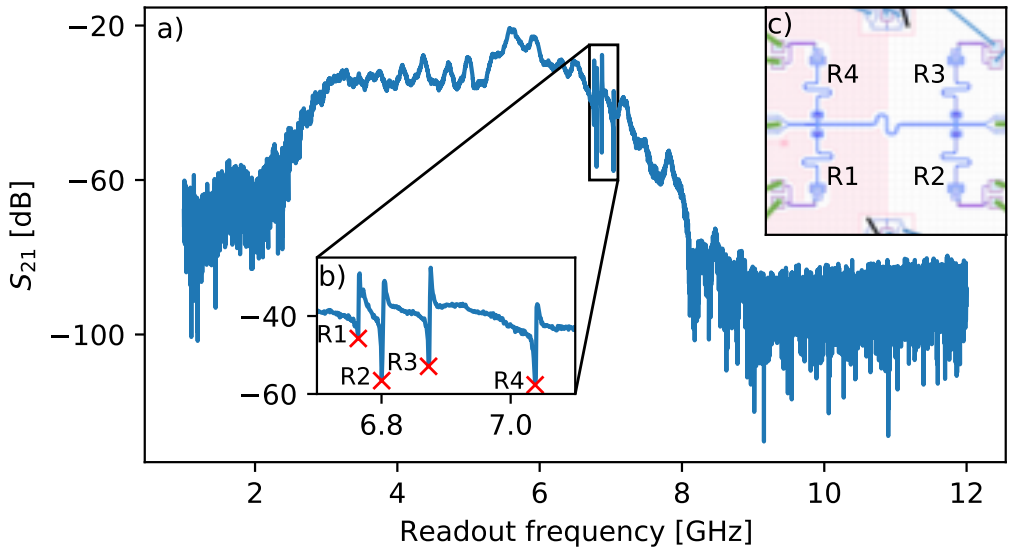

Figure 3.3: Extended frequency sweep. (a) A full frequency sweep ranging from 1GHz to 12GHz. Here a transmittivity plateau was observed, which is due to the bandwidth of the whole readout chain. (b) A zoom-in inset at a frequency window near resonance with local resonator. Four resonance dips were observed. They corresponds to 4 resonators respectively. These four resonators are labelled with R1, R2, R3 and R4 respectively. Right after every resonance dip a transmittivity peak was also observed. This is due to impedance mismatch. (c) Bonding diagram of experiment chip, where 4 resonator are capacitively coupled to the common feedline. The resonance dips of these four resonators are shown in graph (b).

3.1.1 Choice of signal parameters

Before characterizing the TWPA, we need to find out the signal frequency window we are going to work with. We performed a frequency sweep ranging from 1GHz to 12GHz to find the resonance frequency, shown in Fig.3.3 We observed a plateau in the magnitude of the scattering parameter. This is due to the bandwidth of the whole readout chain, e.g. HEMT, room-temperature amplifiers and IQ mixer. On this plateau 4 significant dips were also observed. They correspond to the resonance frequencies of 4 resonators that are connected to the feedline.

After targeting the signal frequency window for resonator frequencies,

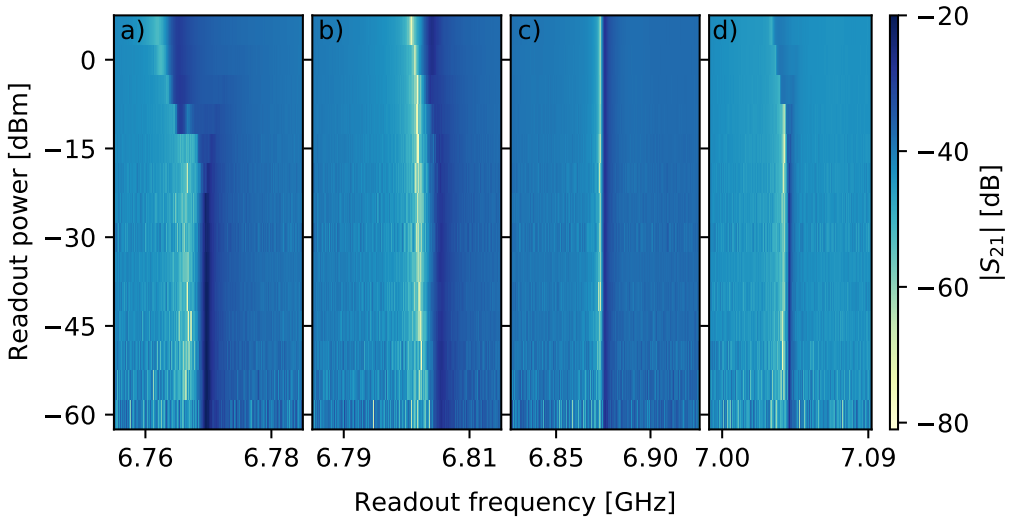

Figure 3.4: Single-tone spectroscopy for all four resonators, where the dark regime represents a resonance dip. From (a) to (d), the four graphs correspond to resonator R1, R2, R3 and R4 respectively, which are also labeled in figure3.3 as well. Here the pulse is denoted as "readout tone", that's because the frequency and power is similar to that of the pulse for qubit readout.

we proceeded to find a suitable signal power. Therefore, we performed a 2D sweep of S_{21} versus readout frequency and readout power. In the 2D map, the dark regime corresponds to the resonator resonance dip. Here we observed a frequency shift of resonator when readout power is above -15dBm. This indicates that the Jaynes-Cummings interaction between qubit and resonator is breaking down, and that this coupling system do not stay at dispersive region any more[23, 1].

As shown in Fig.3.4, for resonator R1, R2 and R4, we observed a frequency shift when readout power reached -10dBm. We also observed the measured resonance dip stayed stable for readout power smaller than -25dBm. While looking for a maximal signal power for the convenience of signal detection without driving the qubit-resonator off their dispersive coupling region, we set the signal tone with power -25dBm for further experiments.

We choose a signal power of -25dBm since this will correspond approximately to the drive strength of the readout resonator in the dispersive qubit readout.

In conclusion, we chose a signal tone with -25dBm power and 6.805GHz frequency(on resonance with R2).

3.1.2 Gain and working point of TWPA

In order to amplify a signal tone, TWPA need an additional pump tone to provide power, whose frequency and power are referred as the "working point" to TWPA. When the pump is turned on/off, we will measure an amplified/un-amplified signal. Therefore, here the gain provided by TWPA is described as the ratio of the signal when the TWPA is on over when the TWPA is off.

To begin with, we performed a wide range 1D sweep of both pump frequency and pump power, as shown in Fig.3.5. This allows us to narrow down the parameter window to execute a finer 2D sweep. For the chosen signal tone of (6.805GHz, -25dBm), we observed that TWPA could provide 20dB gain and above for pump power ranging from -20dBm to -12dBm(Notice that this is the power of signal tone when just leaving the arbitrary wave generator. Due to the attenuation, the signal tone that went into the TWPA is approximately 72dB weaker than its power source, and the pump tone 28dB weaker than its power source.) and for pump frequency ranging from 7.6GHz to 8GHz.

After wide range single-parameter sweep, we proceeded to perform a fine 2D sweep. From the 2D sweep we selected the working point as pump frequency 7.955GHz and pump power -15.5dBm.

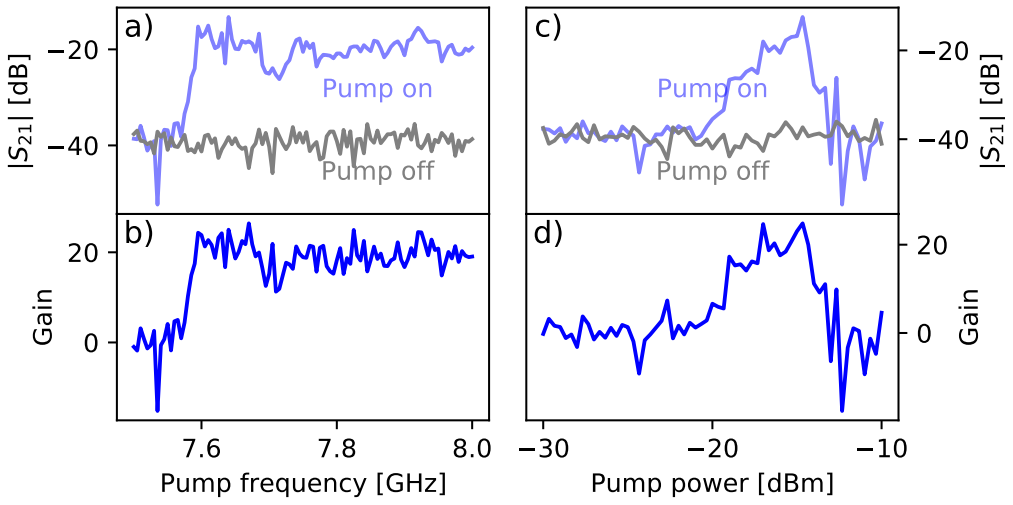

Figure 3.5: Extended single parameter sweep of pump tone (a) Measured $|S_{21}|$ with pump turned on and off versus pump frequency. (b) Measured $|S_{21}|$ when TWPA turned on and off versus pump power. (c) Gain provided by TWPA versus pump frequency. (d) Gain provided by TWPA versus pump power.

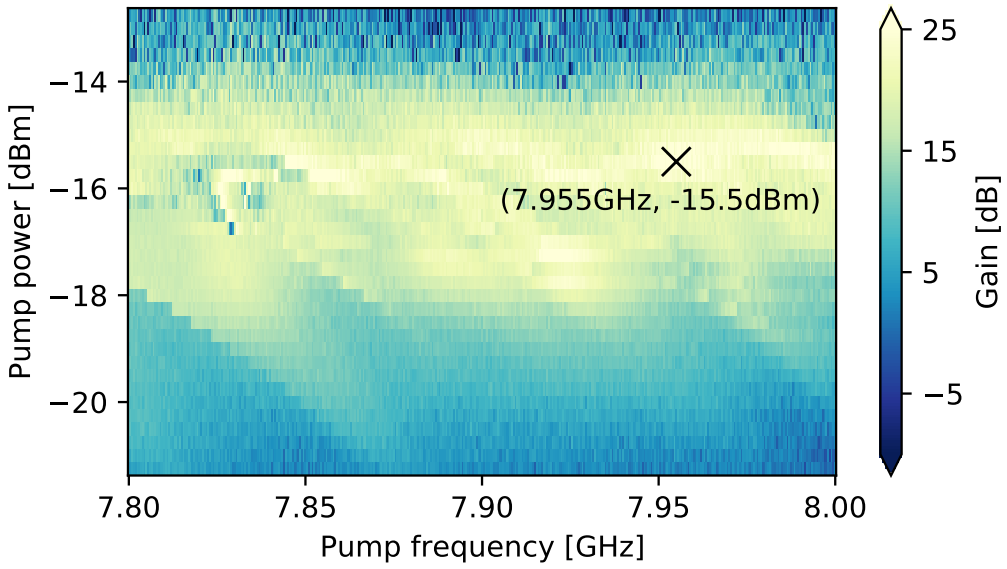

Figure 3.6: Coarse sweep of TWPA's working regime. We find optimal performance at a working point of 7.955GHz frequency and -15.5dBm power.

3.1.3 Bandwidth of TWPA

Bandwidth represent the frequency window of signal in which it can be effectively amplified by TWPA. Since the working point was manually chosen, here we slightly explored TWPA's general bandwidth performance around the chosen working point.

Firstly, we performed a 2D sweep of gain versus signal frequency and pump frequency, as shown in Fig.3.7(a). From the 2D sweep, two data sets were selected and plotted in Fig.3.7(b). One data set corresponds to original pump frequency 7.955GHz, one corresponds to the optimal pump frequency 7.979GHz, where TWPA was observed to provide a higher power gain over a larger signal frequency range. For original pump frequency, TWPA were observed to have a stable amplifying performance above 20dB over the frequency ranging from 6GHz to 7.5GHz, which from figure 3.7 we could see is slightly smaller than the optimal pump frequency.

Secondly, we performed a 2D sweep of gain versus signal frequency and pump power, as shown in Fig.3.8(a). From the 2D sweep, the optimal pump power -15.67dBm was selected and plotted in Fig.3.8(b). The standard for

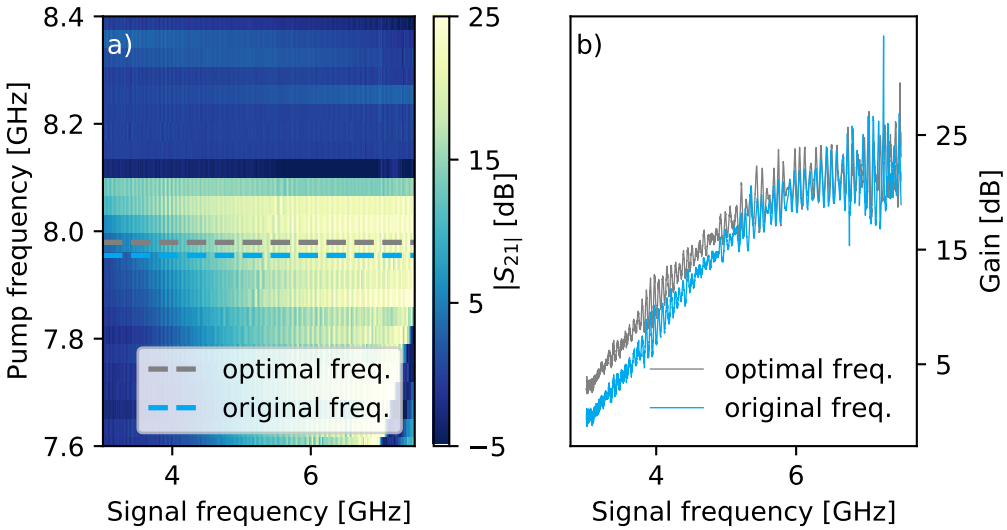

Figure 3.7: 2D sweep of gain versus signal frequency and pump frequency. (a) A 2D sweep with signal frequency window 3-7.5GHz and pump frequency window 7.6-8.4GHz. Here two horizontal lines marks the optimal pump frequency and original selected pump frequency. (b) A 1D-plot of gain versus signal frequency. Here two data set were selected from the 2D sweep, as is marked in (a).

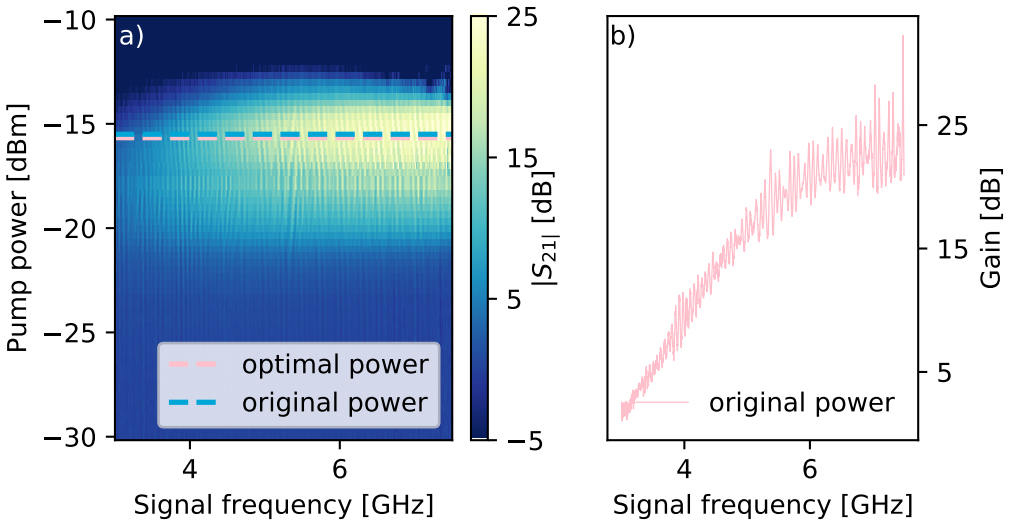

Figure 3.8: 2D sweep of gain versus signal frequency and pump power. (a) A 2D sweep with signal frequency window 3-7GHz and pump power window from -10dBm to -30dBm. (b) Gain versus signal frequency with optimal pump power.This data set corresponds to the dash line marked black in (a)

selection is that TWPA has a stable power gain over the largest signal frequency window. For this optimal pump power -15.67dBm, TWPA were observed to have a stable amplifying performance above 20dB for signal frequency ranging from 6GHz to 7.5GHz. The original pump power was only denoted Fig.3.8(a) and not plotted in (b). This is because that this value is not included in the 2D sweep. However, we could assume that TWPA have a similar performance given the proximity of these two parameter in figure 3.8.

For the chosen working point of (7.955GHz, -15.5dBm) we find a band-width of approximately 1.5GHz. By slightly adjusting the drive tone in frequency and power we are able to reach even better performance as indicated in Fig.3.7 and Fig.3.8 our TWPA for test has near optimal bandwidth performance with the originally chosen working point. In this working point, TWPA could provide a gain above 20dB for a band-width of 1.5GHz. In further experiments, we would continue to use the same working point for TWPA characterization.

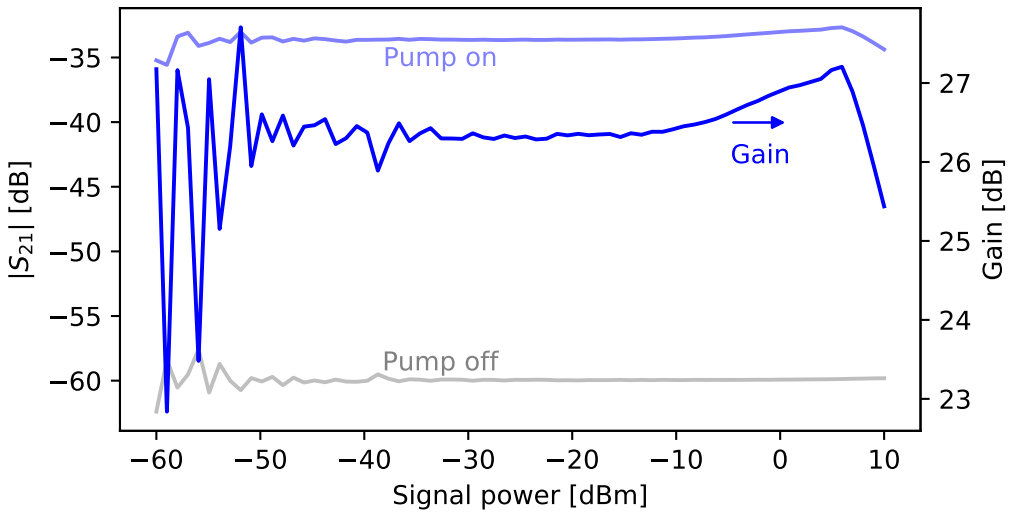

Figure 3.9: Gain versus signal power as well as the measured $|S_{21}|$ versus signal power when pump is turned on and off

3.1.4 Saturation Power of TWPA

Here we performed a 1D sweep of gain versus signal power when setting the TWPA drive to the original working point and signal frequency 6.805GHz that was used to find working point. As shown in Fig.3.9, a severe fluctuation in measurement result was observed for signal power below -40dBm. This was due to the insufficient average time. Meanwhile, an unexpected peak was also observed for signal power around 5dBm.Despite the two aforementioned problems, from the 1D sweep we could still safely conclude that TWPA work stably in the power range of -10dBm to -30dBm.

3.2 Transmon measurements

Our final goal is to characterize the readout system quantum efficiency. This requires the characterization of transmon qubit. In our experiments, we used a nanowire-based transmon, the frequency of which can be tuned through voltage-biasing. The workflow of characterizing transmon is shown in Figure3.10. Firstly, we set the gate-biasing to adjust the qubit frequency of the nanowire-based Transmon and hence the dispersive of the qubit and resonator. Then, we used 1-tone spectroscopy to find the resonator frequency and 2-tone spectroscopy to find the qubit frequency. We iterated the transmon spectroscopy until we fit a transmon frequency more than 2.5 GHz separated from the resonator. Secondly, we performed amplitude Rabi experiment to calibrate the X gate pulse. We continued with the characterize the relaxation time and dephasing time of Transmon qubit. Thirdly, we study the signal distribution for qubit ground state and excited state. A double-Gaussian model was used to fit the histogram. Discriminator between ground/excited state was calibrated. More importantly, SNR and fidelity was extracted.

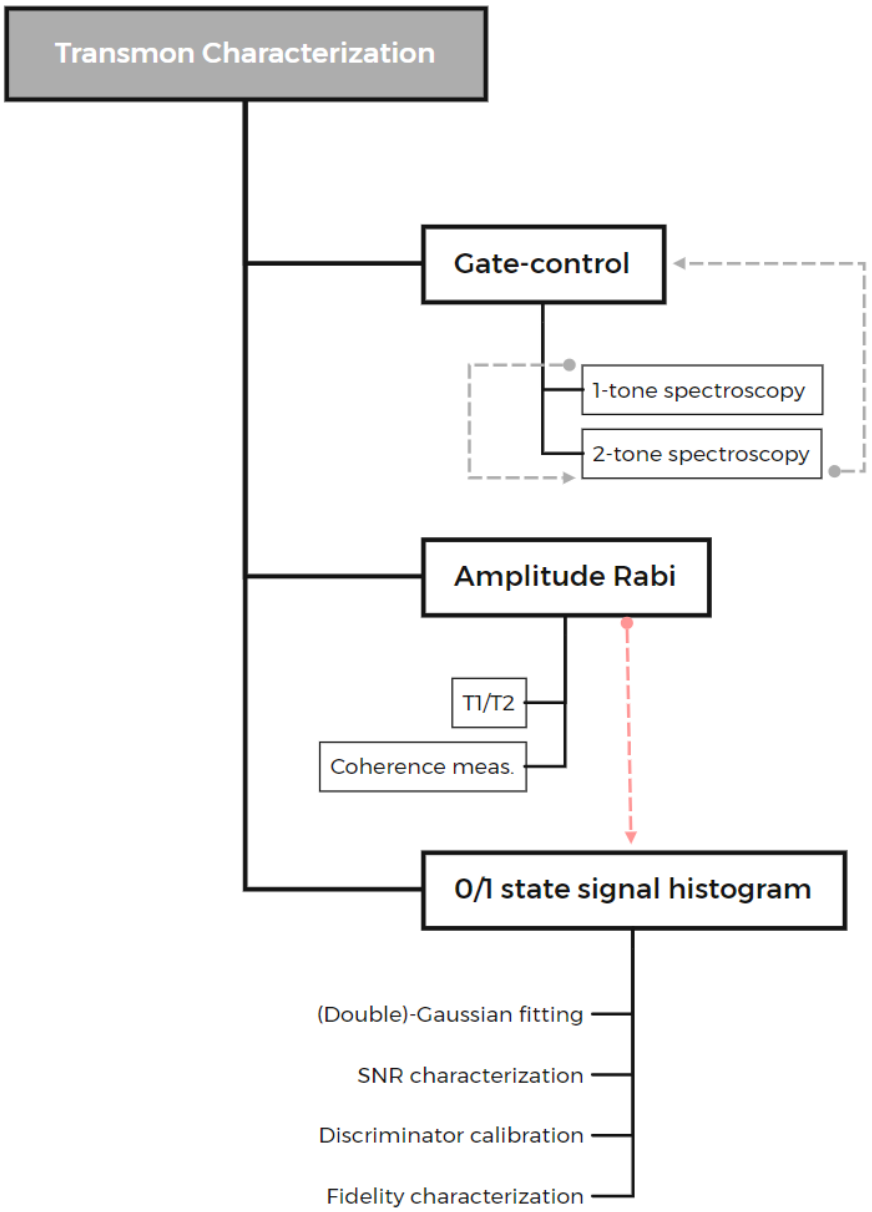

Figure 3.10: Workflow of Transmon characterization. Every box represents an individual experiment. The arrows denote the dependency, where the pink arrow is the most important one.

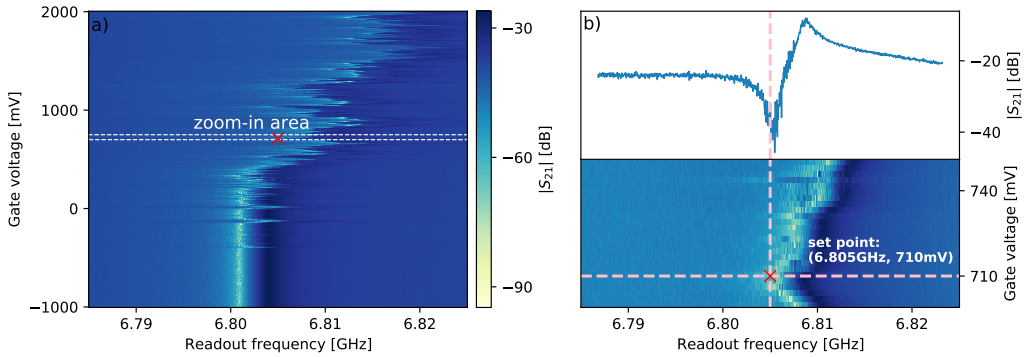

Figure 3.11: Resonator spectroscopy. (a) A wide range sweep of $|S_{21}|$ versus readout frequency and gate voltage, here the dashed window was the parameter range of interest (b) A finer 2D sweep with parameter range denoted as dashed window in (a), the white cross marker denoted the gate biasing we chose for further experiment and the corresponding resonator frequency. (c) A 1D frequency sweep of transmittivity when gate voltage was set to 710mV, the data was chosen from (b). From (c) we measured the resonator frequency as 6.805GHz.

3.2.1 Resonator spectroscopy and gate control of qubit frequency

We scan the signal frequency of the VNA versus the gate voltage applied to the bottom gate of the nanowire Josephson junction, see Fig.3.11 Due to the dispersive coupling between qubit and resonator, the resonator frequency is shifted in response to the change the qubit frequency. The frequency response is non-monotonic due to the microscopic properties of the nanowire junction.

After the spectroscopy we fixed the gate biasing to 710mV such that the resonator and qubit were detuned far enough: The resonator frequency was set to 6.805GHz and the qubit frequency around 4GHz.

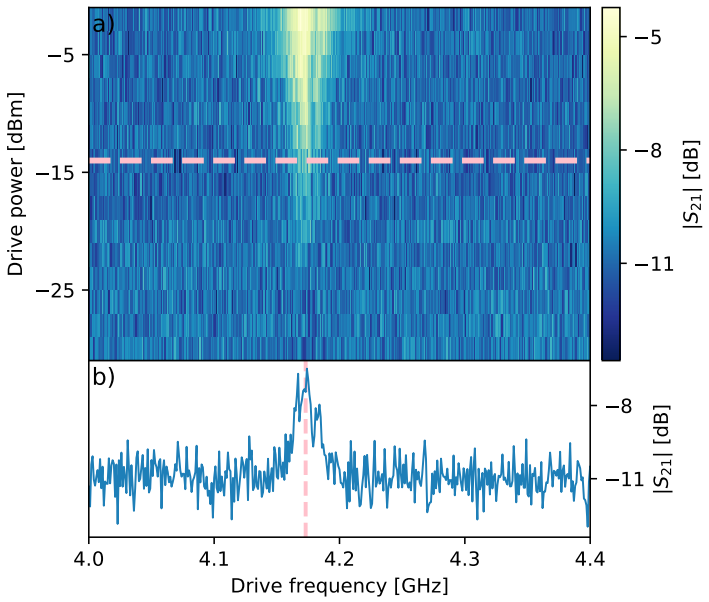

Figure 3.12: 2-tone spectroscopy used to determine qubit frequency. (a) 2D sweep of $|S_{21}|$ versus drive frequency and power. The light yellow region corresponds to the qubit resonance with drive tone. (b) A 1D sweep of readout tone transmittivity versus drive tone frequency. Data was selected from the white dash line in (a), which corresponded to the drive power set to -14dBm. From this 1D sweep we measured the qubit frequency as 4.173GHz.

3.2.2 Use 2-tone spectroscopy to find qubit frequency

We do 2-tone spectroscopy to find the qubit frequency. Firstly, we sent in a continuous wave readout tone at resonance frequency of the resonator. Secondly, we apply a drive tone with variable power and frequency near the eigenfrequency of the qubit, see Fig.3.12. From the 2D map we observed a regime with higher transmission. This is the regime where the drive tone is on resonance with qubit transition frequency, i.e., where the drive tone can effectively flip the qubit into excited state. When flipped into a different state, the qubit would pull resonator off its original resonance, causing an inversion of transmittivity observed. Since our resonance corresponds to a transmission dip, the peak of transmission peak in this 2D spectroscopy corresponds to the qubit resonance with the drive.

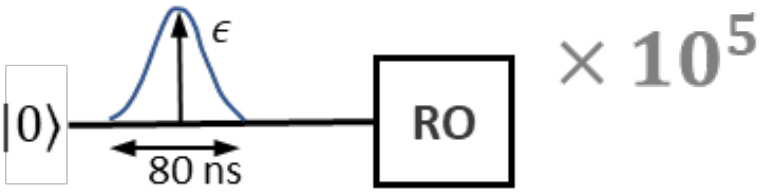

Figure 3.13: Amplitude Rabi experiment

3.2.3 Amplitude Rabi experiment

After finding the resonator frequency and qubit frequency. We are able to perform an amplitude Rabi experiment. The pulse schedule is shown Fig.3.13. We sent in a Gaussian pulse to drive the qubit to the excited state of the qubit. This drive pulse has a fixed drive frequency that is on resonance with qubit transition frequency, a fixed drive length of 80ns, and a variable drive amplitude. Right after the drive pulse, we sent in a readout pulse that is on resonance with the resonator and then measured the readout signal. For every drive amplitude we repeat the process for 10^5 times and then averaged the measured signals. The averaged signal corresponds to the expectation value of qubit state created by that drive amplitude. When plotting all the results together, we observed an oscillation of measured signal versus drive amplitude. The drive amplitude corresponding to half a period yields the required drive strength for a pi-pulse.

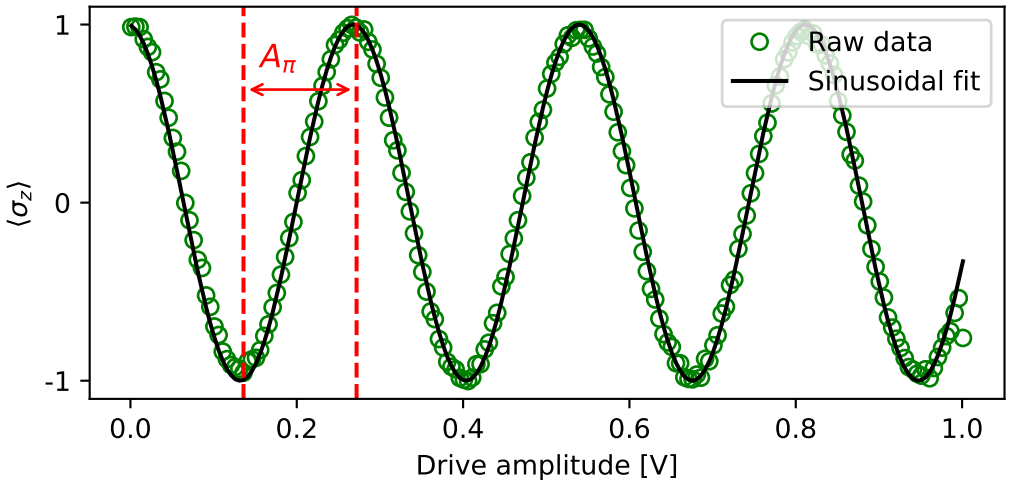

Figure 3.14: Amplitude Rabi experiment. Here the average signal was normalized to correspond to the expected value of qubit state. The fitting is a simple sinusoidal model $S(t) = A\sin(Bx + \phi) + C$

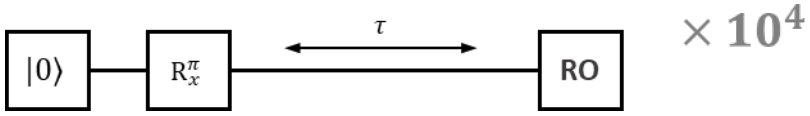

Figure 3.15: T1 experiment pulse schedule

3.2.4 Measure relaxation time T1

Here we characterized the time scale in which a qubit will decay from excited state into ground state. When increasing the time interval, we observed an exponential decay of average signal(proportional to $\exp[-t/T_1]$), which corresponds to the change of qubit population. Fitting model is described in Eq.2.25. We characterized the relaxation time T1 as $1.220\mu s$.

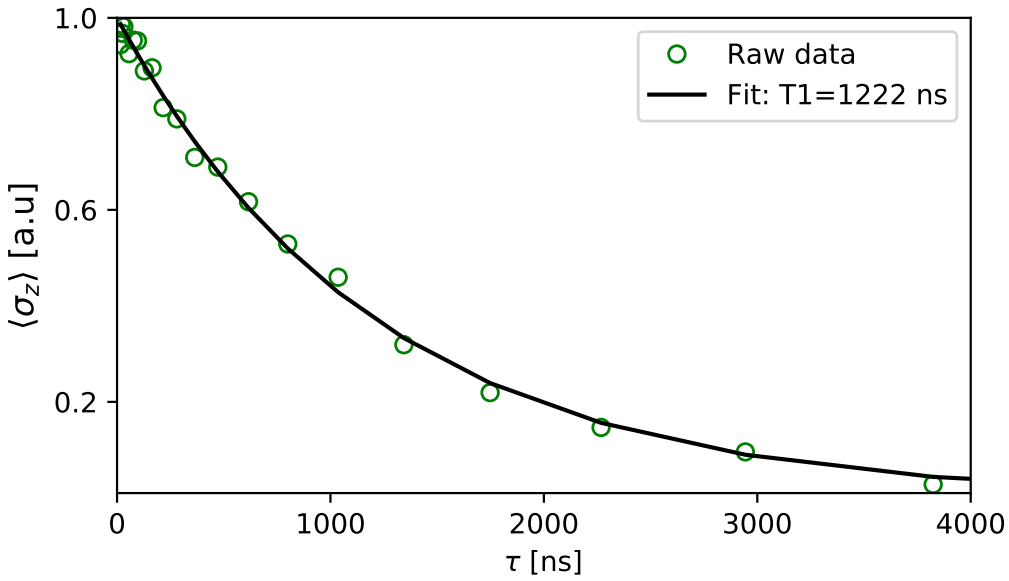

Figure 3.16: Relaxation time measurement. Fitting gave a relaxation time T_1 of 1222ns.

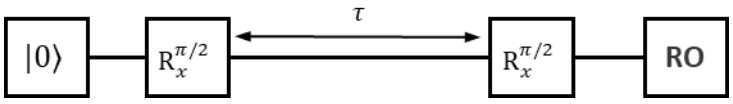

Figure 3.17: T2 experiment pulse schedule

3.2.5 Measure dephasing time T2

We implemented a Ramsey pulse sequence to measure dephasing time T2 of the qubit. This pulse sequence consists of two separated pi/2 pulse with a variable interval time τ in between. Before the Ramsey experiment, we prepared qubit in ground state, injected the Ramsey pulse sequence and then measured the qubit. The pulse schedule is shown in Fig.3.17 We observed a decayed oscillation of the measured signal with respect to the time interval τ.

Characterizing T2 requires a good fitting of this decayed oscillation. Here we chose a fitting model with tunable decaying profile, as described with coefficient n in Eq.2.26. This fitting gave a dephasing time $T_2 = 224ns$ and

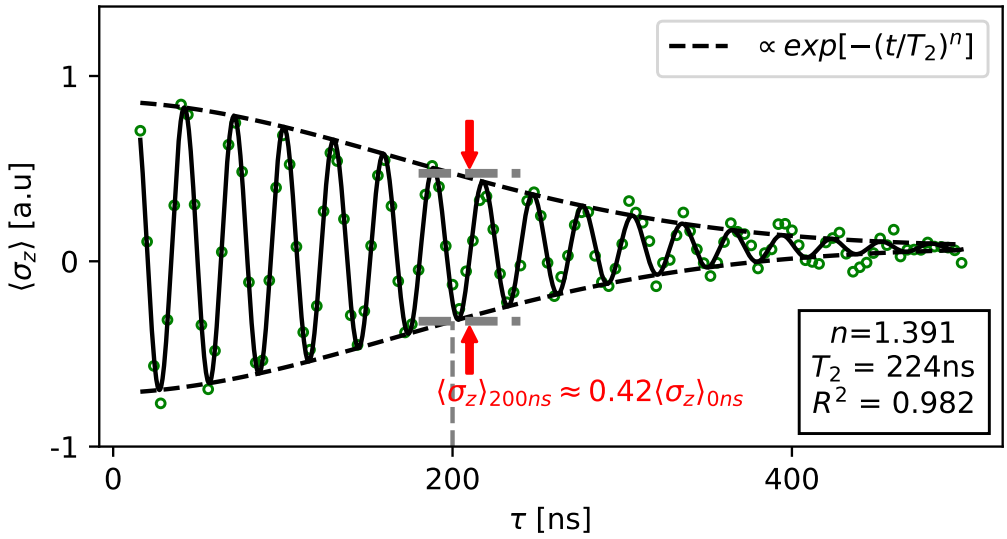

Figure 3.18: Ramsey experiment with fitting, where R^2 denotes the coefficient of confidence.

decaying profile $\exp[-(t/T_2)^n]$ with $n = 1.391$, as shown in Fig.3.17. The Ramsey time T_2 contains information n both energy relaxation and pure dephasing T_ϕ in the qubit, i.e., $1/T_2 = 1/(2T_1) + 1/T_\phi$. Therefore, the pure dephasing time T_ϕ can be extracted as $T_phi = 246ns$. The fact that T_phi is much shorter than T_1 and the fact that decaying profile $n > 1$ indicate an existence of strong dephasing channel that leads to strong qubit frequency fluctuation, as observed in Subsec.3.2.7.

In the later experiments, we studied the remaining coherence of qubit after subjecting to a weak readout pulse of fixed pulse length. Therefore, the pulse length should be short than the dephasing time T_2, or otherwise the contribution of dephasing from the weak readout pulse would become indiscernible. Looking only at raw data at delay time 200ns, we observed that there was still approximately 42% of coherence remained, as denoted in Fig.3.18. Therefore, we assumed that qubit still remain sufficiency coherence for experiment after 200ns of dephasing.

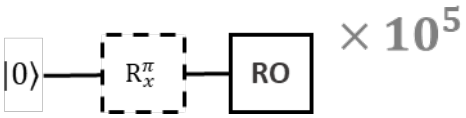

Figure 3.19: Experiment design to study qubit state signal probability distribution

3.2.6 Signal calibration: Discriminator, SNR and fidelity

By studying the signal distribution of single-shot measurements $\bar{z}_{|0\rangle/|1\rangle}$, we could characterize the readout chain's performance with SNR and fidelity. We did this by repeatedly prepare qubit in ground/excited state and measure it right after using a strong, long square pulse(1000ns pulse length, 0.12V pulse amplitude), as shown in Fig.3.19

The resulting signal distribution in I-Q plane is shown in Fig.3.20(a). For each qubit state, we observed that the population of measured signal in the phase space can be divided into one major blob and one subsidiary blob that partially overlap with each other. While the major blob corresponds to the correct signal of corresponding qubit state, the subsidiary blob corresponds to the signal of residual opposite qubit state. Those residual states could either due to the failure to correctly prepare qubit state or due to the unwanted state transition or relaxation behavior during the measurement process.

Fig.3.20(b) shows the rotated signal distribution, this is equivalent to performing a integral with square weight function, as is explained in subsection 2.3.6 This rotation maximized the difference between ground state signal and excited state signal in horizontal direction, as denoted in Fig.3.20(e). From Fig.3.20(f) we observed that there still remains some difference in the vertical direction. This could be due to the existence of higher level. By using only the I component for qubit state discrimination, the noise from higher level could then be eliminated.

After projecting all the information into the I-quadrature, we proceeded to count the distribution of measured signal and then perform double-Gaussian fitting. The histogram of the measured signal and fitting are shown in Figure 3.21. As for the fitting model, the main Gaussian represents the qubit state of interest and the subsidiary Gaussian represents the residual qubit state. Ignoring the influence of higher-level qubit state, we expect that the main Gaussian positions and subsidiary Gaussian positions that corresponds to

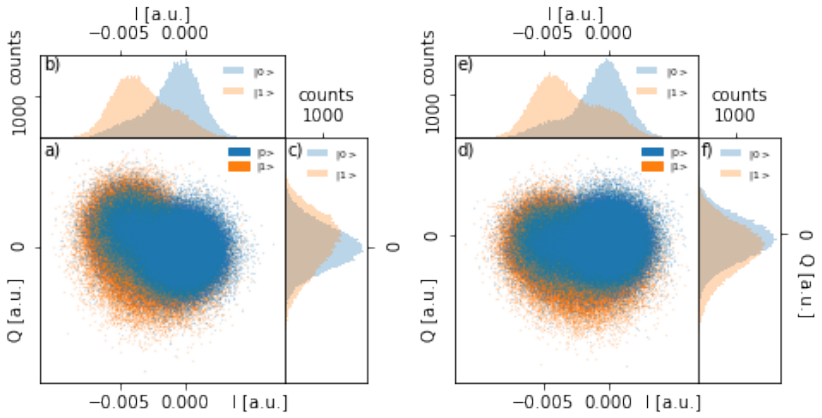

Figure 3.20: Measured signal represented in phase-space.
(a)I-Q representation of signal population.(b) and (c) describes the distribution in single one component of all dots in (a).
(d)Rotated phase-space representation of signal population.(e) and (f) describes the distribution in single one component of all dots in (d).

ground state and excited state should align with each other. From the fitting in Figure3.21(b) we also observed that excited-state signal distribution has a larger subsidiary Gaussian than that of the ground state. This is because that excited state could decay to ground state due to qubit relaxation in addition to the measurement induced transition.

Here we performed fitting for both signal distribution individually. Then we checked the alignment of Gaussian peaks between ground and excited signals, as denoted as the vertical line in (b).

The discriminator could be used to differentiate ground state signal from excited state signal. The discrimination error, or the measurement error, is then denoted in the overlap of the distribution for the two qubit states.

Here the signal is defined as the distance between the main Gaussian for $|0\rangle$ and $|1\rangle$.

After double-Gaussian fitting in Fig. 3.21(b), we calibrated the discriminator that differentiates ground state signal from excited state signal. Then the measurement error could be defined as the signal that appears in the "wrong" side of the discriminator, as shown in Figure 3.21(c). From measurement error we calculated the fidelity for this measurement. The result value is 0.425. It is worth noting that the calibration of the discriminator is

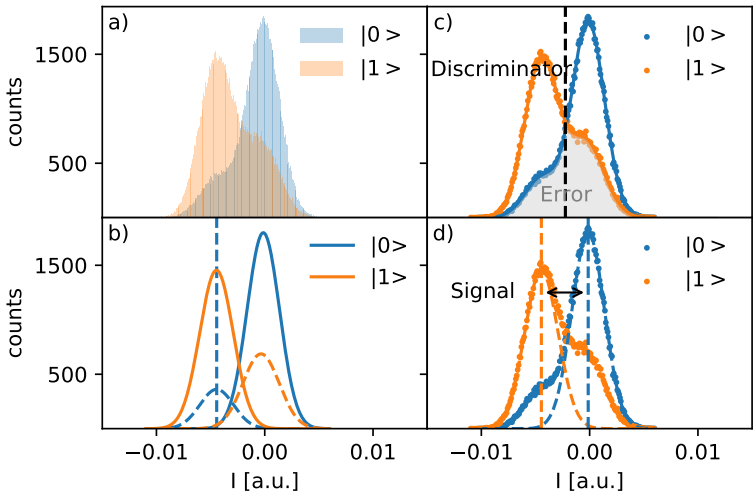

Figure 3.21: Histogram and fitting of measured signal. (a)Histogram of 10^5 shots for ground state signal and excited state signal respectively. (b)Double-Gaussian model for both ground state signal and excited state signal. (c)The intersection point of fitted curve for both states is used to define the discriminator. The measurement error is denoted in grey area(d)The definition of the signal.

not the main purpose of this thesis project, but a way to double-check the correctness of obtained single-shot measurement distribution, as in Fig.3.30

Apart from measurement error and fidelity, we also calculated the signal-to-noise ratio (SNR) of the measurement. As in Fig. 3.21(d), here is the signal is defined as the distance between the two main Gaussian and the noise is defined by averaging the standard deviation of excited and ground state signal.

3.2.7 Qubit frequency instability and frequency shifting

During the measurement, we noticed that the qubit frequency unstable in time. As shown in Fig.3.22, we monitored the change of qubit frequency within one hour. We observe that for only half of the time the qubit frequency stays within a fixed window between 4.08GHz and 4.10GHz. The biggest jump between two records are up to 300MHz and the standard deviation of

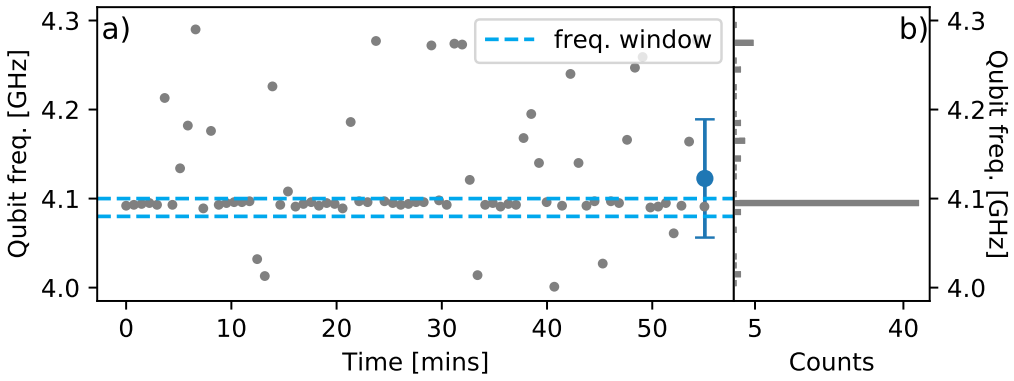

Figure 3.22: A qubit frequency log in 1 hour. (a) 75 qubit frequency measurement data points in 55 minutes. From the graph, we measured a average qubit frequency of 4.123GHz with 66MHz standard deviation, which is denoted in the error bar. We observed a frequency window of width 20MHz. Histogram in (b) showed that approximately half the counts lied in this window. It also showed that qubit with frequency outside the frequency window is unstable because of the few repeatability. Therefore, we argued that the frequency window encompasses qubit's bare frequency, whereas the drastic frequency jumping is a result of external noise.

the measured data set reaches 66MHz. We also observed that the frequency jumping usually happened within 3 minutes, since the data points were taken approximately every 0.75 minutes and from Fig.3.22 we observed 4 incidence within the stable window in a row. This frequency jumping is problematic since all the further measurements individually take about the same time of 3-4 minutes and there's large change that the frequency jumping will undermine the gate fidelity during.

One potential cause of this frequency jumping is the existence of charge noise. Using a python package called QuTiP[49], we studied the influence of charge noise by simulating the transmon Hamiltonian described in Eq.2.27. However, simulation of Transmon's Hamiltonian revealed that the charge noise could not explain the 300MHz jump range but only the width of frequency window(approximate 20MHz), as denoted in charge noise, as shown in Fig.3.23. Meanwhile, the charge noise couldn't explain the distribution of qubit frequency. As shown in Fig.3.23(b), charge noise would result in a bipolar distribution of qubit frequency, which is exactly the opposite of the

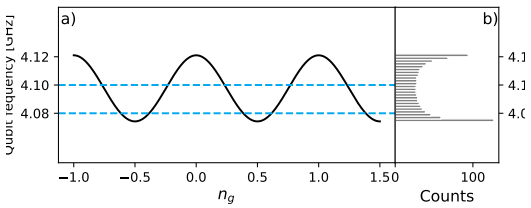

Figure 3.23: Simulation of qubit frequency at the influence of charge noise. Here capacitive energy E_C is set to 450MHz, and the ratio E_J/E_C is tuned into 13.12, as shown in Table 3.2.8.

real situation. Therefore, we excluded the charge noise on the transmon as the cause of frequency jumping. On the other hand, the charge noise (or charge jumps) on the gate-control line of the qubit could cause this observed qubit jumping in principle. The real source of noise that caused this observed qubit fluctuation required more inspection.

Apart from the problem of sudden frequency jumping, there was one additional problem that was related. For most of the time, the qubit tends to stay within a fixed frequency window with a width of 20MHz. However, we noticed, that this frequency window also drifts over time. In Fig. 3.24 we show the qubit transition frequency versus time on two different days. We observed that the frequency window drifted by 7MHz. Despite the problem of window drifting, we assumed that frequency window would remain stable on the time scale of a few hours.

Let me outline the problem of the frequency drift again: The calibration of pi-pulse requires the exact knowledge of the qubit frequency. That means, if the qubit frequency changes after the the pi-pulse was calibrated, the original pi-pulse could no longer successfully flip the qubit into excited state. Therefore, a direct result of any qubit frequency jumping is that we fail to obtain the correct signal distribution that corresponds to the excited

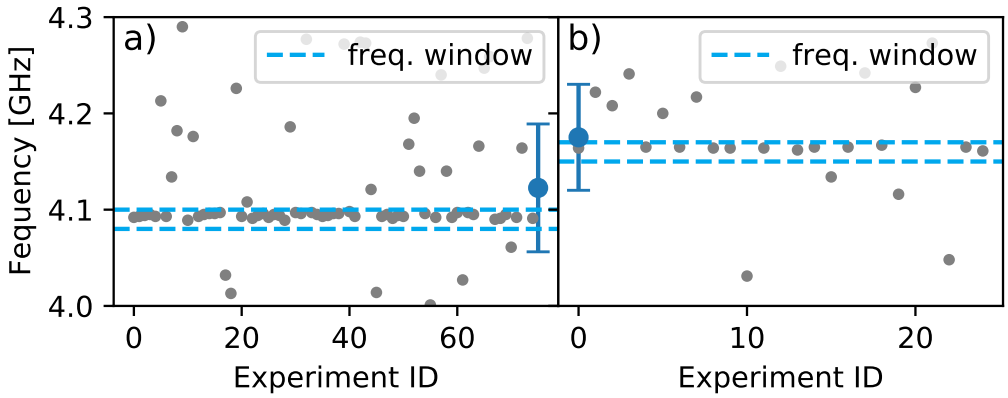

Figure 3.24: Two collection of qubit frequency in two different days. We observed that the frequency window drifted from [4.08GHz, 4.10GHz] to [4.15GHz, 4.17GHz].

state. Fig. 3.25 shows the resulting signal distribution for five independent qubit state signal histogram experiments with the same readout pulse(500ns pulse length, 0.31V pulse amplitude). In the insets, we plot two dots denote the measured qubit frequency before and after a single experiment. We also plotted two blue lines to denote the stable frequency window. We observed that when the qubit frequency was off the stable window, we completely lose the signal population that corresponds to excited state, as shown in Figure 3.25(a) and (c). This is because that there is very few chance for qubit to stay stable at the same frequency outside the frequency window. This statement is supported by the histogram in Figure 3.22(b).

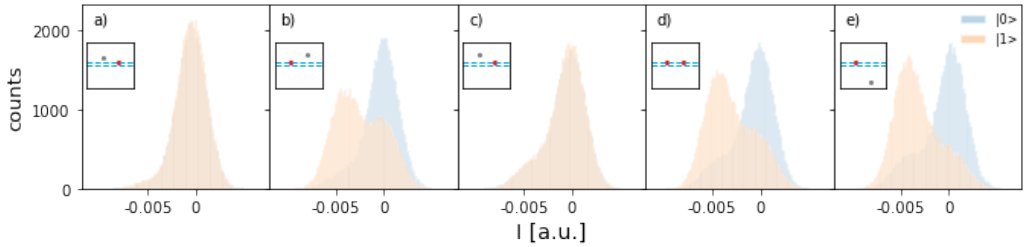

Figure 3.25: Five repeated experiments to determine signal distribution. The insets depict the qubit frequency before and after experiments and the stable frequency window. The frequency record within the window is plotted a red dot

3.2.8 Summary

Below is a table for the measured quantities of Transmon qubit. Here the resonator frequency and qubit frequency is measured with a large standard deviation, the data comes from Figure3.29(b) and (c). The Josephson energy E_J, capacitive Energy E_C and coupling strength g are pre-measured value.

Quantity	Value
T_1	$1.222\mu s$
T_2	224ns
f_r	6.805±0.001GHz
f_q	4.160±0.068GHz
E_c	0.45GHz
E_J	5.903GHz
E_J/E_c	13.12
g	250MHz

3.3 Quantum efficiency

Here we use the 3-step method introduced by Bultink el al. to characterize the quantum efficiency of the readout chain. As described in subsection2.3.10, when working in weak measurement regime, SNR is expected to scale linear, $SNR = a\epsilon$, and qubit coherence is expected to exhibit a Gaussian dependence, $|\rho_{01}(\epsilon)| = A \cdot \exp\left(-\frac{\epsilon^2}{2\sigma_m^2}\right)$. Then system's quantum efficiency could be measured as:

$$\eta = \frac{\sigma_m^2 a^2}{2}. \tag{3.1}$$

It is worth noting that the 3-step method has 2 preconditions: 1) optimal integration functions are used to optimally extract information from both quadratures, and 2) the intra-resonator field vanishes at the beginning and end. However, here in our experiment the square weight integration functions were used. This would result in a relatively smaller Quantum Efficiency[14].

3.3.1 Experiment design

This section explained the experiments carried to extract quantum efficiency. Two topic were discussed here: First one is about choosing the readout pulse with suitable pulse length, second one is about using frequency sifting to remove untrustworthy data.

Choice of readout pulse

To begin with, we need to choose a readout pulse for the variable strength measurement. For the sake of simplicity, a square pulse envelope was chosen here. However, the choice of pulse length requires more scrutiny.

The pulse length should be chosen such that we could measure both SNR and qubit coherence afterwards with a range of different readout amplitude. On the one hand, the pulse length should be shorter than the dephasing time T2, or otherwise the qubit will completely lose it's coherence even the pulse amplitude equals zero. On the other hand, the pulse length should be long enough so that we could measure at least some signal difference between state $|0\rangle$ and state $|1\rangle$. As illustrated in Fig. 3.18(c), the qubit could still remain 40% of coherence after 200ns of dephasing. Therefore, here we choose the pulse length as 200ns.

X gate calibration and data-sifting based qubit frequency

Given the fact that our qubit frequency was jumping at least in a timescale of 5 minutes, as shown in 3.22, and the fact that it is the same time scale to perform a single SNR measurement and coherence measurement, we re-calibrate the X-gate pulse amplitude before every experiment. This requires the re-calibration of resonator frequency and qubit frequency. Therefore, for every single SNR/coherence experiment, we calibrated the resonator frequency and qubit frequency, then we calibrated the X gate amplitude, then we prepare the qubit in the state and perform the measurements.

Since those single experiments are performed consecutively, for every experiment we could know the qubit frequency before and right after the measurement. This allowed us to perform a post-measurement selection based of whether the qubit was in the stable frequency window that was mentioned in section 3.2.7.

In conclusion, we used square pulse with fixed pulse length 200ns and variable pulse amplitude to perform the weak measurement. We studied the change of SNR with respect to different readout amplitude(SNR measurements), and studied different readout amplitudes' impact on qubit's coherence using Ramsey sequence(Coherence measurements). For every individual experiment, qubit frequency was recorded before and after. Those records were used for post-measurement data selection. The whole experiment process is depicted in Figure3.26.

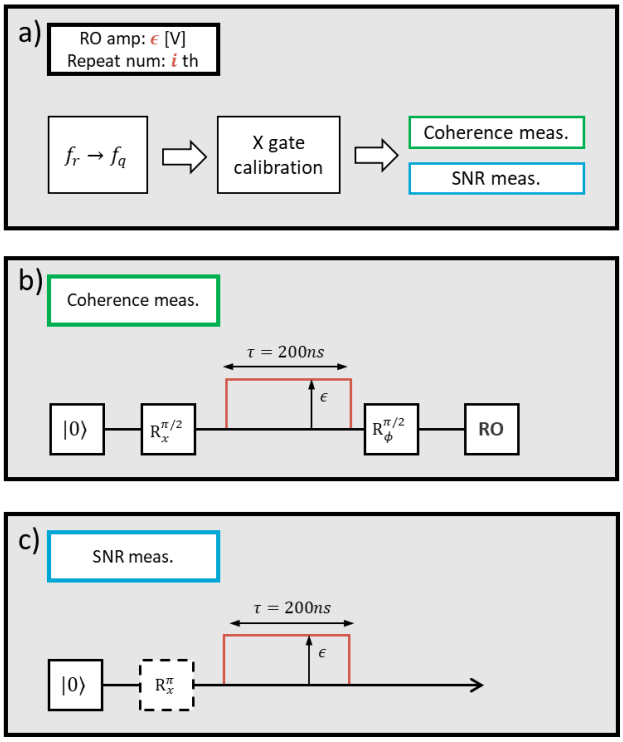

Figure 3.26: Quantum efficiency experiment design. (a)General process to perform a SNR/coherence experiment. (b)Pulse schedule for coherence experiment. Here "RO" represent a strong measurement to fully collect qubit's coherence. (c)Pulse schedule for SNR measurement. Notice that no additional "RO" is needed here, but to collect all the scattered signal of the weak pulse that's injected.

3.3.2 Measurement result

SNR measurement versus readout amplitude ϵ

In total 300 SNR experiments were carried here, where 30 different readout amplitude ranging from 0V to 0.2V were used, and for every readout amplitude the experiment was repeated for 10 times. When increasing the readout amplitude, we observe an increase in the separation of two signal distribution for ground and excited state, as shown in Figure 3.28.

The histogram for the excited/ground state usually fit a double-Gaussian fitting. This is due to the existence of projection error. As shown in Figure 3.27, the measurement pulse could cause unwanted state transitions. Meanwhile, the excited state could decay into ground state due to qubit's natural relaxation.

However, here we used single-Gaussian model for the fitting of signal histogram. The legitimacy of this use was argued in the later part of this sub-subsection.

Here we performed a frequency sifting to eradicate those experiments

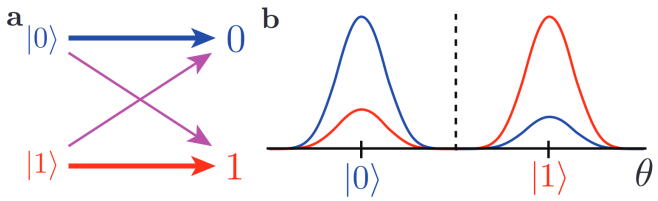

Figure 3.27: Illustration of qubit state projection and double-Gaussian distribution of measured signal[16]. (a)Illustration of qubit state projection between the qubit state and measured state. Here the projection error is denoted in purple. (b)Corresponding double-Gaussian probability distribution of single-shot measurement value $\bar{z}_{|0\rangle/|1\rangle}$

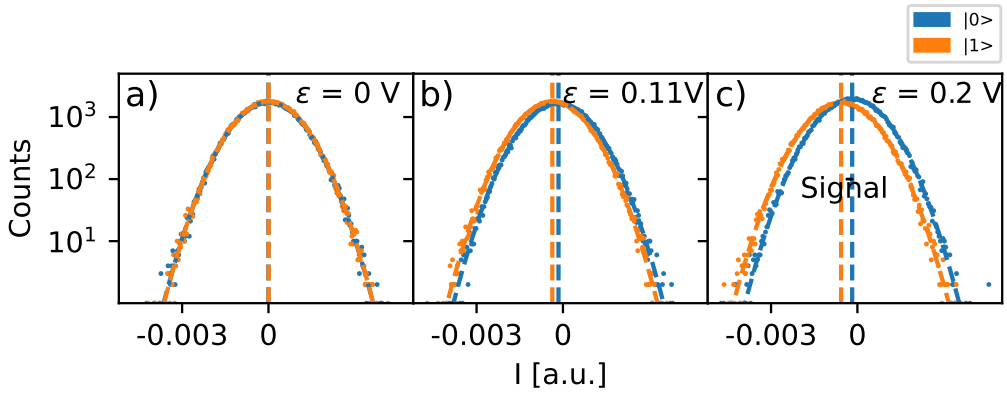

Figure 3.28: SNR measurement versus different readout amplitude. Here we inject a square readout pulse with pulse length of 200ns. By varying the readout amplitude ϵ from 0V to 0.2V we observed a slight shift between the signal distribution for $|0\rangle$ and $|1\rangle$. In the weak measurement regime, we fitted the data with single-Gaussian model.

where qubit frequency has jumped drastically. The frequency sifting criteria states that the qubit frequency before and after qubit state should lie within the stable window that was observed in that experiment series. Using this criteria, 67 out of 300 SNR experiments were selected, and the results were plotted in Figure 3.29.

As mentioned before, single-Gaussian model was used in the process of extracting SNR from signal histograms. The calculation of determination coefficient R^2 showed a good fit of single-Gaussian model, the result is shown in Figure 3.30(a). Furthermore, according to [44], the measurement fidelity should be related to the SNR by $F_m = 1 - erfc(SNR/2)$ if the state signal distributions are single Gaussian, where F_m and SNR are two quantities that can be extracted independently from the signal histogram. Here we extracted the SNR for signal distributions and then computed the expecting Fidelity. The result showed a good match with the actual measured Fidelity, as shown in Figure 3.30(b).

Here we argued the legitimacy of using single-Gaussian model for the fitting of signal histograms. There are two reasons that support this usage:(i), the readout process(200ns) is much shorter than the relaxation time(1200ns) such that few excited states would decay into ground state. (ii), the readout pulse is too weak to populate the ground state into excited state due to both its short duration and low amplitude. To prove our argument that, we performed a series of stronger measurement as shown below.

For the stronger measurement that has longer readout pulse length and readout pulse amplitude, we implemented a square readout pulse with pulse duration of 500ns and pulse amplitude ranging from 0.25V to 0.5V. The measurement time is long enough for qubit relaxation and pulse strength is strong enough for state-transition. Here we observed a double-Gaussian distribution. The alignment of main Gaussian and subsidiary Gaussian supported supports the hypothesis, that only two states are involved here. As seen in Fig. 3.31(a), subsidiary Gaussian for $|1\rangle$ is higher than that of $|0\rangle$. This is reasonable because $|1\rangle$ has one more channel to transition into $|0\rangle$ during measurement, as shown in Figure3.27. When the readout amplitude was increased further, there were more $|0\rangle$ to $|1\rangle$ state transition, which would account for the increase of subsidiary Gaussian for $|0\rangle$. On the other hand, the decrease of subsidiary Gaussian for $|1\rangle$ could be because that the excited state is further excited into non-computational basis.

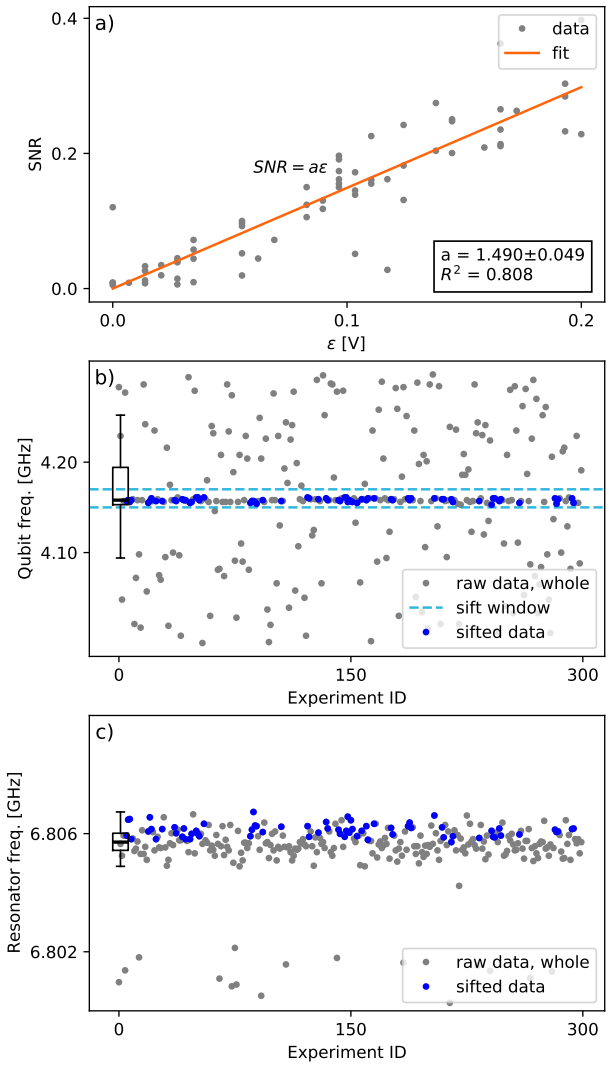

Figure 3.29: SNR measurements result.
(a)Extracted SNR versus different readout amplitude.
(b) Qubit frequency records. The box plot in the left shows that near half the qubit frequency records stayed at the frequency window [4.15GHz,4.17GHz]
(c)Resonator frequency records. In contrast to qubit frequency, the resonator stayed relatively stable with only 1MHz of fluctuation.

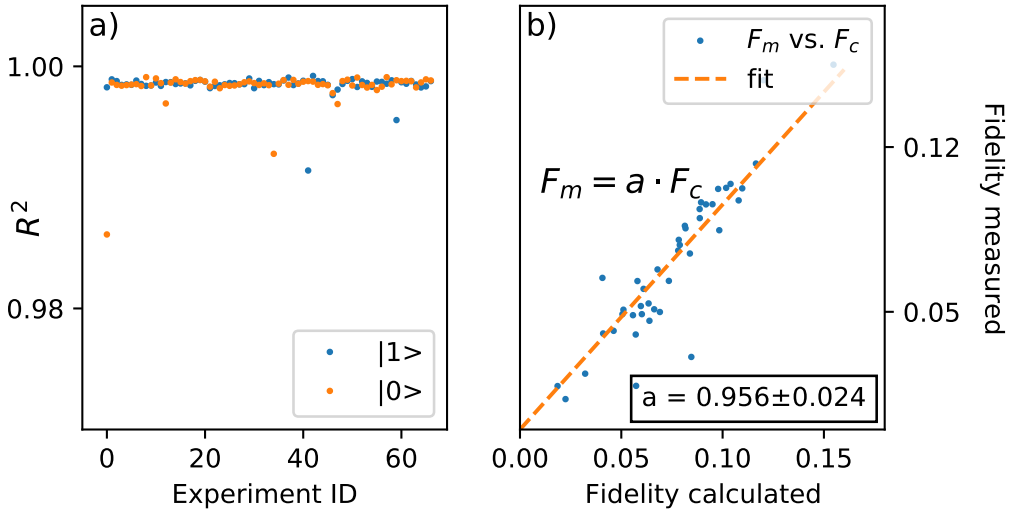

Figure 3.30: Evaluation of fitting result of SNR. Those data points corresponded to the data points in 3.29(d). (a) Coefficient of determination R^2 for using single-Gaussian fitting model. (b) The measured fidelity versus calculated fidelity using single-Gaussian fitting model. Notice that the calculation involved a slightly different definition of SNR, which is defined in Eq. 2.41

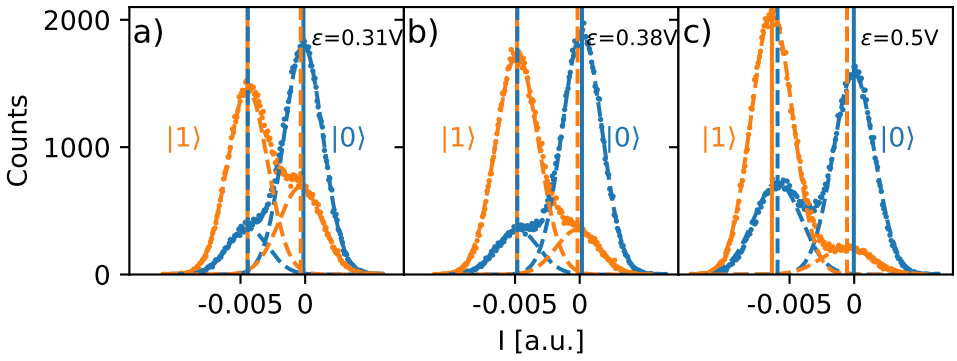

Figure 3.31: Histograms of 3 strong measurements. For readout amplitude ranging from 0.3V to 0.5V, a change in the relative height of two subsidiary Gaussian was spotted. The reason that the ground state signal has an even higher subsidiary Gaussian for ϵ=0.5V could be because excited state $|1\rangle$ got excited into higher level.

Coherence measurement versus readout amplitude ϵ.

We used Ramsey experiment to measure the remaining coherence of qubit. We did this by inserting the weak readout pulse between the 2 pi/2-pulse. The pulse sequence is shown in Figure 3.26. To increase the accuracy the measured coherence, we rotated the azimuthal angle ϕ of the second pi/2-pulse until we could measure the coherence to the fullest. As shown in Fig. 3.32, an increase in the readout amplitude would lead to more dephasing of qubit coherence.

In the coherence measurement, two data sets obtained at different time of the same day were stacked together for the analysis. Together there are 91 raw data points in total, whose corresponding readout power ranges from $0V$ to $0.03V$. From the raw data points 34 data points were chosen using the frequency sifting mentioned in sub-subsection3.3.1. From the sifted data we observed that the remaining qubit coherence for every readout amplitude has a ceiling value, and that the ceiling value experienced a Gaussian decays with respect to the increment of readout amplitude. Here we postulated that those under-ceiling coherence value is a signature of frequency jumping, which could be modeled as the influence of the environment noise. Therefore, after performing a frequency sifting for both data sets, we selected the ceiling values out of those data points and performed a decay fitting so to calculate the quantum efficiency. From the fitting we observed that coherence was already completely destroyed when readout amplitude reached 0.04V. The results together with the qubit frequency and resonator frequency records were shown in Figure 3.33

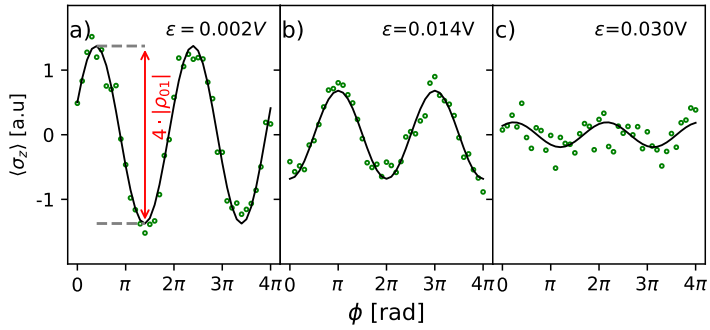

Figure 3.32: Coherence measurement result versus different readout pulse. We observed a rapid decreasing of coherence while increasing the readout amplitude from 0V to 0.03V, as denoted from (a) to (c).

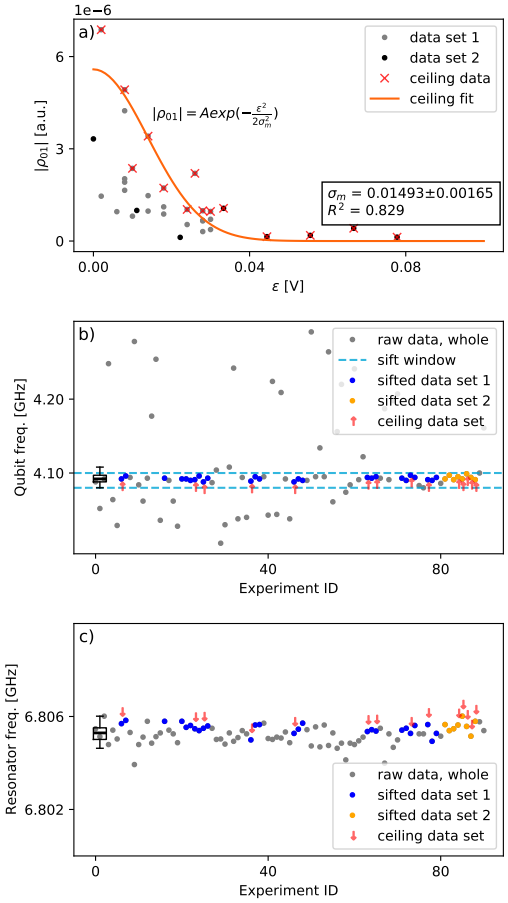

Figure 3.33: Coherence measurement result
(a)Coherence measurement versus readout amplitude.
(b)The qubit frequency log for all coherence measurement. The stable frequency window is [4.08GHz, 4.10GHz], as shown in box plot.
(c) Resonator frequency record for coherence measurements. Unlike qubit frequency, the resonator frequency remained stable at frequency window of 2MHz.

Quantum efficiency and converted noise temperature

Bringing the results from the SNR measurements and coherence measurements together, we were able to extract the quantum efficiency of the whole readout system. Using the formula 3.1, we extracted the value as $\eta = 0.002145 \pm 0.000529$.

The quantum efficiency is also related to the system's noise temperature through the formula $\eta = \frac{\hbar\omega_r}{k_B T_{sys}}$. We extracted the system noise temperature to be $T_{sys} = 15225 \pm 3754K$. This is a temperature three times hotter than the surface of sun. This abnormal value indicated either the existence of a strong internal source of noise of the measurement chain or the failure to collect and amplify the signal.

To target the internal source of noise, the dilution refrigerator was opened. While no obvious problem was revealed in the cryogenic part of measurement chain, an severe instability was spotted in the amplifier response. As shown in Figure3.34, the range of gain could fluctuate up to 30dB(from blue and red). Meanwhile, the amplifier response was spotted to undergo an abrupt jump when the connecting cable was touched or even someone stepping around without touching anything.

The conclusion is that there exists one or more bad contacts in the room-temperature measurement chain. Those bad contacts account for the fluctuation of amplification response. It could be the case that those data points were acquired when the system response is trapped at some wire configuration with very low gain. This assumption could explain the low SNR and henceforth the low quantum efficiency. Further examination has been being carried.

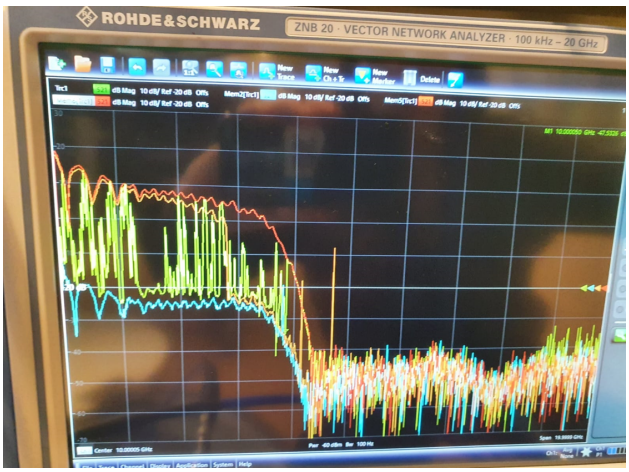

Figure 3.34: System amplification response over a short period of time. With the same experiment condition, the system gain could fluctuate at a level of 30dB, between the bottom blue lie and top red line.

Chapter 4

Conclusion and Outlook

Conclusion

In this work, we have set the basis for the characterization of superconducting parametric amplifier. Using TWPA as the amplifier to test, this research entailed two sections: The basic and the advanced characterization. The basic characterization focused on the gain, bandwidth and saturation power of TWPA. A series of qubit characterization experiments were carried out as well. They served as a preparation for the advanced characterization, which characterization focused on extracting the quantum efficiency of the whole qubit readout chain where TWPA is installed.

Using a VNA, we had performed a series of basic TWPA characterization experiments. We started by setting the signal frequency and power that resemble the actual qubit readout. After setting the input signal, we found the optimal working point for TWPA. For this working point we characterized the three basic figures of merits for TWPA: gain, bandwidth, and saturation power. From the result we concluded that TWPA stays in its optimal working configuration in the case of qubit readout.

Using VNA and OPX, we had performed a series of basic transmon qubit characterization experiments. These experiments mainly served as a preparation for the characterization of quantum measurement efficiency of the readout chain. We performed: resonator spectroscopy for resonator frequency, qubit spectroscopy for qubit frequency, amplitude Rabi experiment for pi-pulse characterization, T_1 and T_2 measurement, fidelity and Signal-to-Noise ratio (SNR) characterization, and qubit frequency tracking. In cases where the readout signal population was expected to obey Gaussian distribution,

the fidelity and SNR were used to compared with each other to check if the signal distribution is Gaussian or not [23]. The fact that dephasing time T_2 is much shorter than relaxation time T_1 indicated that there exists a strong dephasing channel, one contribution of which would be the frequency fluctuation of the qubit[12]. In support of this argument, we observed a drastic qubit frequency jumping at a frequency range of 300MHz and in the time scale of at least minutes, where there existed a relatively stable frequency window of width 20MHz. According to the numerical modeling[49], we showed that the charge noise could neither account for the range of frequency jumping nor the distribution of observed qubit frequency. The real source of noise remain unknown.

Using the 3-step method developed by Bultink et al.[14], we have extracted the quantum efficiency of the qubit readout chain. We performed a series of SNR characterization with respect to different amplitude of the weak readout pulse. The readout pulse length was adjusted to be 200ns, which is slightly shorter that the qubit dephasing time T2. Using a strong readout pulse, we also measured the remaining coherence of the qubit after subjecting to the weak readout pulse for SNR characterization. We performed a post-measurement data sifting based on the qubit frequency before and after each individual measurement. From the remaining data we extracted the system's quantum efficiency of approximately 0.002, a value that is much lower than the state-of-art[1]. This low quantum efficiency value arises from the low SNR and strong qubit dephasing. On the one hand, the strong qubit dephasing corresponded to the unknown noise source that caused drastic qubit frequency jumping. On the other hand, the low SNR, according to the latest experiment setup examination, could be attributed to the unstable room-temperature amplifier response and poor cable connection.

In summary, we had established a complete and replicable workflow with written code for the characterization of a general quantum limited amplifier. The reusable code included the control of the pulse sequence and data analyzing in the complete characterization process. To highlight the contribution of the author of this thesis, the code for data analyzing and partially pulse sequence control of OPX was developed by Master student Duiquan Zheng. We had also targeted two major problem in the qubit readout chain. Once a better experiment setup is available, the quantum limited amplifier that is currently being developed by Lukas Splitthoff in Andersen Lab could be characterized immediately.

Outlook

For the outlook, there exists a list of things that could be done in the future. The goal is to improve SNR, to reduce qubit dephasing strength, and to strengthen the credibility of quantum measurement efficiency.

To begin with, the problems of unstable amplifier response and poor cable connection need to addressed. Another big problem is about the drastic qubit frequency jumping. The noise source that cause the qubit fluctuation needs to be targeted and eradicated.

On the other hand, if the noise source locates somewhere in the original qubit chip(QPP-5p5-rev4), it is tempting to fabricate and install a new qubit that is more resilient to environmental charge noise. One other motive to fabricate a new qubit chip is to improve the SNR. To date, a transmon qubit that is more suitable for characterizing amplifier had been being designed and simulated. With a larger $E_J/E_C = 32$, this new transmon qubit is more resilient to charge noise. An unsymmetrical coupling of the resonator increases the efficiency of collecting readout signal. To further this project, this newly designed transmon could be fabricated.

One other thing to improve the SNR is to optimize the readout pulse by tuning the pulse frequency and pulse envelope[1]. For example, the pulse envelope could be tailored such that it accelerated the photon depletion of the resonator. Meanwhile, for the readout signal demodulation, the optimal weight function is also a must, because it is a precondition for the robust extraction of the quantum efficiency of the system[14].

To improve the credibility of the extracted quantum efficiency, an independent method to extract quantum efficiency should be carried out in the future. There exists a method to extracts the quantum efficiency of the system[15], a method that implements the stark-shift effect of the qubit. This method could be carried out in the same readout chain configuration. By implementing this parallel method to extract the quantum efficiency of the readout chain and comparing it to the quantum efficiency extracted using the original method, the credibility of the result would be strengthen.

Since this project focuses on the characterization of a quantum-limited amplifier. It is reasonable to try to extract the quantum efficiency of the amplifier-to-test in the future. This could be done by using a three-stage model[14], which determines the contribution of each individual components to the quantum efficiency of the readout chain.

Acknowledgement

This project is a collective work contributed by many researchers in Andersen Lab and Kouwenhoven lab at Qutech. Many thanks to Arno Bargerbos, Marta Pita Vidal, Vukan Levajac, and Lukas Splitthoff for the help with the code to control OPX. Many thanks to Marta Pita Vidal, Jaap Wesdorp, and Lukas Splitthoff for the debugging of measurement station. Many thanks to Arno Bargerbos for his insight on the nanowire transmon. Many thanks to my thesis Christian Kraglund Andersen for his insight on my thesis project, especially the motivation. Finally, tons of thanks to my daily supervisor Lukas Johannes Splitthoff for his patience, his faith on me, and his support throughout the research and life.

Bibliography

[1] Yvonne Y Gao et al. "A practical guide for building superconducting quantum devices". In: *arXiv preprint arXiv:2106.06173* (2021).

[2] Jose Aumentado. "Superconducting parametric amplifiers: The state of the art in Josephson parametric amplifiers". In: *IEEE Microwave Magazine* 21.8 (2020), pp. 45–59.

[3] Saptarshi Chaudhuri et al. "Broadband parametric amplifiers based on nonlinear kinetic inductance artificial transmission lines". In: *Applied Physics Letters* 110.15 (2017), p. 152601.

[4] Daniel J Parker et al. "A near-ideal degenerate parametric amplifier". In: *arXiv preprint arXiv:2108.10471* (2021).

[5] Luca Planat et al. "Understanding the saturation power of Josephson parametric amplifiers made from SQUID arrays". In: *Physical Review Applied* 11.3 (2019), p. 034014.

[6] TC White et al. "Traveling wave parametric amplifier with Josephson junctions using minimal resonator phase matching". In: *Applied Physics Letters* 106.24 (2015), p. 242601.

[7] Luca Planat et al. "Photonic-crystal Josephson traveling-wave parametric amplifier". In: *Physical Review X* 10.2 (2020), p. 021021.

[8] Tsuyoshi Yamamoto et al. "Flux-driven Josephson parametric amplifier". In: *Applied Physics Letters* 93.4 (2008), p. 042510.

[9] B Yurke et al. "Observation of parametric amplification and deamplification in a Josephson parametric amplifier". In: *Physical Review A* 39.5 (1989), p. 2519.

[10] Florian Luthi et al. "Evolution of nanowire transmon qubits and their coherence in a magnetic field". In: *Physical review letters* 120.10 (2018), p. 100502.

[11] Patrick Harvey-Collard et al. “Circuit quantum electrodynamics with two remote electron spins”. In: *arXiv preprint arXiv:2108.01206* (2021).

[12] Philip Krantz et al. “A quantum engineer’s guide to superconducting qubits”. In: *Applied Physics Reviews* 6.2 (2019), p. 021318.

[13] Luca Planat. “Resonant and traveling-wave parametric amplification near the quantum limit”. PhD thesis. Université Grenoble Alpes [2020-....], 2020.

[14] Cornelis Christiaan Bultink et al. “General method for extracting the quantum efficiency of dispersive qubit readout in circuit QED”. In: *Applied Physics Letters* 112.9 (2018), p. 092601.

[15] Chris Macklin et al. “A near–quantum-limited Josephson traveling-wave parametric amplifier”. In: *Science* 350.6258 (2015), pp. 307–310.

[16] Christopher Stewart Macklin. *Quantum feedback and traveling-wave parametric amplification in superconducting circuits*. University of California, Berkeley, 2015.

[17] Sh Barzanjeh, DP DiVincenzo, and BM Terhal. “Dispersive qubit measurement by interferometry with parametric amplifiers”. In: *Physical Review B* 90.13 (2014), p. 134515.

[18] David M Pozar. *Microwave engineering*. John wiley & sons, 2011.

[19] Hermann A Haus and JA Mullen. “Quantum noise in linear amplifiers”. In: *Physical Review* 128.5 (1962), p. 2407.

[20] Hermann A Haus. *Electromagnetic noise and quantum optical measurements*. Springer Science & Business Media, 2000.

[21] Carlton M Caves. “Quantum limits on noise in linear amplifiers”. In: *Physical Review D* 26.8 (1982), p. 1817.

[22] Aashish A Clerk et al. “Introduction to quantum noise, measurement, and amplification”. In: *Reviews of Modern Physics* 82.2 (2010), p. 1155.

[23] Alexandre Blais et al. “Circuit quantum electrodynamics”. In: *Reviews of Modern Physics* 93.2 (2021), p. 025005.

[24] DI Schuster et al. “ac Stark shift and dephasing of a superconducting qubit strongly coupled to a cavity field”. In: *Physical Review Letters* 94.12 (2005), p. 123602.

[25] A Bruno et al. "Reducing intrinsic loss in superconducting resonators by surface treatment and deep etching of silicon substrates". In: *Applied Physics Letters* 106.18 (2015), p. 182601.

[26] M Stoutimore Khalil et al. "An analysis method for asymmetric resonator transmission applied to superconducting devices". In: *Journal of Applied Physics* 111.5 (2012), p. 054510.

[27] MD Reed et al. "High-fidelity readout in circuit quantum electrodynamics using the Jaynes-Cummings nonlinearity". In: *Physical review letters* 105.17 (2010), p. 173601.

[28] Zhongyuan Zhou, Shih-I Chu, and Siyuan Han. "Quantum computing with superconducting devices: A three-level SQUID qubit". In: *Physical Review B* 66.5 (2002), p. 054527.

[29] Thorvald Wadum Larsen et al. "Semiconductor-nanowire-based superconducting qubit". In: *Physical review letters* 115.12 (2015), p. 127001.

[30] Arno Bargerbos et al. "Observation of vanishing charge dispersion of a nearly open superconducting island". In: *Physical review letters* 124.24 (2020), p. 246802.

[31] Chen Wang et al. "Surface participation and dielectric loss in superconducting qubits". In: *Applied Physics Letters* 107.16 (2015), p. 162601.

[32] Oliver Dial et al. "Bulk and surface loss in superconducting transmon qubits". In: *Superconductor Science and Technology* 29.4 (2016), p. 044001.

[33] Gianluigi Catelani et al. "Quasiparticle relaxation of superconducting qubits in the presence of flux". In: *Physical review letters* 106.7 (2011), p. 077002.

[34] Simon Gustavsson et al. "Suppressing relaxation in superconducting qubits by quasiparticle pumping". In: *Science* 354.6319 (2016), pp. 1573–1577.

[35] Evan Jeffrey et al. "Fast accurate state measurement with superconducting qubits". In: *Physical review letters* 112.19 (2014), p. 190504.

[36] Shay Hacohen-Gourgy et al. "Quantum dynamics of simultaneously measured non-commuting observables". In: *Nature* 538.7626 (2016), pp. 491–494.

[37] S Touzard et al. “Gated conditional displacement readout of superconducting qubits”. In: *Physical review letters* 122.8 (2019), p. 080502.

[38] Andrew Eddins et al. “Stroboscopic qubit measurement with squeezed illumination”. In: *Physical review letters* 120.4 (2018), p. 040505.

[39] Nicolas Roch et al. “Observation of measurement-induced entanglement and quantum trajectories of remote superconducting qubits”. In: *Physical review letters* 112.17 (2014), p. 170501.

[40] Nicolas Didier, Jérôme Bourassa, and Alexandre Blais. “Fast quantum nondemolition readout by parametric modulation of longitudinal qubit-oscillator interaction”. In: *Physical review letters* 115.20 (2015), p. 203601.

[41] Carlton M Caves et al. “Quantum limits on phase-preserving linear amplifiers”. In: *Physical Review A* 86.6 (2012), p. 063802.

[42] Colm A Ryan et al. “Tomography via correlation of noisy measurement records”. In: *Physical Review A* 91.2 (2015), p. 022118.

[43] Theodore Walter et al. “Rapid high-fidelity single-shot dispersive readout of superconducting qubits”. In: *Physical Review Applied* 7.5 (2017), p. 054020.

[44] Jay Gambetta et al. “Protocols for optimal readout of qubits using a continuous quantum nondemolition measurement”. In: *Physical Review A* 76.1 (2007), p. 012325.

[45] DH Slichter et al. “Measurement-induced qubit state mixing in circuit QED from up-converted dephasing noise”. In: *Physical Review Letters* 109.15 (2012), p. 153601.

[46] Maxime Boissonneault, Jay M Gambetta, and Alexandre Blais. “Dispersive regime of circuit QED: Photon-dependent qubit dephasing and relaxation rates”. In: *Physical Review A* 79.1 (2009), p. 013819.

[47] Daniel Sank et al. “Measurement-induced state transitions in a superconducting qubit: Beyond the rotating wave approximation”. In: *Physical review letters* 117.19 (2016), p. 190503.

[48] Michael Simoen et al. “Characterization of a multimode coplanar waveguide parametric amplifier”. In: *Journal of Applied Physics* 118.15 (2015), p. 154501.

[49] J Robert Johansson, Paul D Nation, and Franco Nori. "QuTiP: An open-source Python framework for the dynamics of open quantum systems". In: *Computer Physics Communications* 183.8 (2012), pp. 1760–1772.